ISSN 1883 - 0315

TOHOKU UNIVERSITY

IMR KINKEN Research Highlights 2024

Institute for Materials Research, Tohoku University

Research

KINKEN

Research Highlights

2024

Institute for Materials Research, Tohoku University

KINKEN Research Highlights 2024

Contents

3. Electronic Materials

Research Centers

G : GIMRT (Global Institute for Materials Research Tohoku) is a program in which researchers from inside and outside the institute conduct joint research based on a common research theme.

I : International Co-Authored Paper

Research

Preface

Dear Colleagues,

We are delighted to present “KINKEN Research Highlights 2024,” our annual report that showcases research findings from the Institute for Materials Research (IMR) at Tohoku University for the past year. KINKEN is the abbreviation for “Kinzoku Zairyo Kenkyusho,” the Japanese name for IMR, and is well known in the materials science community.

IMR has a rich history spanning over one hundred years since its establishment in 1916. Initially, the focus was on iron and steel materials, but as times changed and research progressed, its scope expanded to include the fundamentals and applications of various materials, including non-metals such as semiconductors and ceramics. With these changes, the institute changed its name from the Research Institute for Iron, Steel and Other Metals (RIISOM) to the current one in 1987. Ever since Dr. Kotaro Honda, its first director, invented the world’s first artificial permanent magnet called KS magnet steel, the institute has developed many new materials for practical use, including Sendust alloy, SiC fibers, and soft magnetic amorphous alloys, and has also conducted not only fundamental research, but also pioneering research in the search for new materials and the elucidation of physical properties such as magnetism and superconductivity. It has become a global center in materials science.

A key feature of IMR is its integration of fundamental and applied research, as well as science and engineering fields. Additionally, the institute stands out for its joint research with both domestic and international researchers, utilizing world-class facilities for experiments (high-energy irradiation testing, high magnetic fields, supercomputers, etc.) and for the creation and evaluation of new materials. In

Takahiko Sasaki

Director Prof. Takahiko Sasaki

2018, IMR was certified as the International Joint Usage/Research Center for Materials Science, known as “Global Institute for Materials Research Tohoku” (GIMRT). IMR is committed to further promoting research and fostering the next generation of researchers, and putting into practice Dr. Honda’s words, “Industry is the training ground of academics,” it also focuses on the likes of industry-academia collaboration and engineer training.

IMR is committed to creating a sustainable society, a goal shared by the global community. Its materials science research has the power not only to solve issues but also to positively transform society. The institute is dedicated to supporting the international competitiveness of Japan’s materials manufacturing and engaging in global endeavors to create academic intellectual property shared by humankind. IMR will continue to work on innovative materials science research that will bring about a paradigm shift with a long-term vision and contribute to developing human resources who will lead the future.

We hope KINKEN Research Highlights will provide insights into our recent research activities and help encourage worldwide collaboration with IMR. We value your continued support and welcome any suggestions.

Infrastructural Materials

IMR KINKEN Research Highlights 2024

Neutron Proved Time-Temperature-Dependent Structural Transformation in a Medium-Entropy Alloy

We have succeeded in observing direct evidence of time-temperature-dependent short-/long-range structural transformation in a medium-entropy alloy. The results of neutron-scattering experiments show that a ternary equiatomic alloy, Mn-Co-Ni, transforms from a face-centered cubic to a primitive tetragonal structure only in a limited time-temperature region. Our findings are possibly available to control elusive short-range ordering in random solid solutions.

The concept of high-entropy alloys has been received in various fields, such as structural materials, catalysts, and the synthesis of new superconductors. Although short-range ordering plausibly plays a crucial role in material properties, the clear correlation has never been demonstrated. In particular, it is generally difficult to probe the short-range ordering via any microscopic experiments and thus the characterization of short-range ordered structure is a frontier issue for the field of high-entropy alloys. In this report, we introduce parts of our research for a possible short-range ordered alloy, Mn-Co-Ni [1,2].

The polycrystalline samples of Mn-Co-Ni were prepared via the arc melting method. Parts of the samples were annealed at several temperatures and then examined through neutron-scattering techniques. The neutron experiments were carried out using a conventional triple-axis spectrometer, TOPAN, which was installed at the 6G horizontal beam port in JRR-3.

As shown in Fig. 1, the as-grown Mn-Co-Ni (black circles) shows a clear diffuse scattering around the forbidden (100) reflection point, indicating a short-range ordered structure in this alloy. Indeed, the roughly evaluated correlation length of the short-range superlattice structure is approximately 1.3(1) nm, which is shorter than that of the average structure evaluated from a width of the fundamental (200) Bragg peak.

The effect of aging at 673 K is displayed in Fig. 1 (left). The broad peak becomes sharper with aging time and splits into two peaks, indicating the development of a long-range tetragonal phase ($L1_0$). The evaluated correlation length is almost resolution-limited (~40 nm) above 147.9 h. The evolution of the diffuse scattering was only observed in a limited temperature range of around 673 K, as shown in Fig. 1 (right). This behavior can be explained with a time-temperature-transformation diagram schematically illustrated in Fig. 2. These findings indicate that short-/long-range ordering forms in the

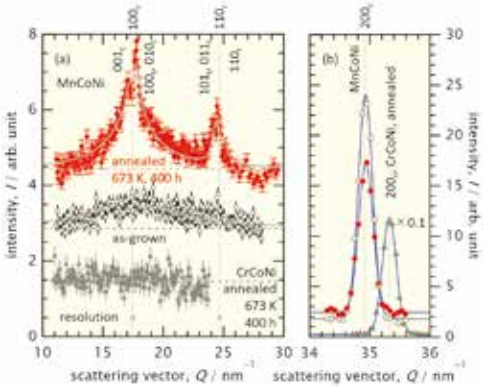

Fig. 1 Neutron-scattering profiles of a medium-entropy alloy, Mn-Co-Ni. The left panel shows the isothermal evolution of the diffuse scattering profile, and the right panel displays the temperature variation for selected temperatures. These figures are cited from Ref. [1].

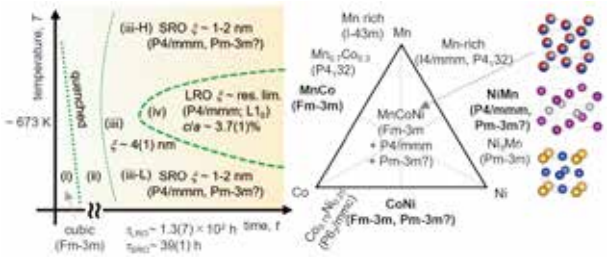

Fig. 2 A schematic time-temperature-transformation diagram of a medium-entropy alloy, Mn-Co-Ni.

Mn-Co-Ni alloy and is available to control with simple heat treatment. The relationship between such characteristic structures and material properties, such as precipitation hardening and novel transport properties, is of subsequent natural interest.

References

[1] Y. Umemoto, Y. Ikeda, and M. Fujita, Mater. Trans. **64**, 2018 (2023).

[2] Y. Ikeda, Y. Umemoto, D. Matsumura, T. Tsuji, Y. Hashimoto, T. Kitazawa, and M. Fujita, Mater. Trans. **64**, 2254 (2023).

Yoichi IKEDA (Quantum Beam Materials Physics Research Laboratory)
E-mail: yoichi.ikeda.d2@tohoku.ac.jp
URL: http://qblab.imr.tohoku.ac.jp/index-e.html

GIMRT

Sublattice Alloy Design of High-Strength Steels

The sublattice alloy design in high-strength steels is proposed with emphasizing nanoscale dispersion control of alloy carbides/nitrides in ferrite. The study uncovers interstitial–substitutional solute interactions revealing hidden nanoscale inhomogeneity via spinodal ordering. The concept of interstitial sublattice engineering is introduced for strengthening alloyed steels in bulk and at surface.

Metallic material strengthening has been a focal research area, addressing dislocation motion challenges posed by microstructure obstacles. Recent studies emphasize severe plastic deformation's role in dislocation and grain-boundary strengthening, while precipitation strengthening remains crucial for achieving high strength. Our research group explores nanoscale inhomogeneity in apparent solid solutions, ordering / phase separation during thermal processes, and a novel alloy design concept called "interstitial sublattice engineering" for strengthening alloyed steels [1].

Carbon (C) and nitrogen (N) occupy interstitial sublattice sites in an iron (Fe) lattice, leading to various carbides / nitrides. Most of them have the crystal structure different from the matrix, and coherency between the α and precipitates is difficult to maintain, resulting in heterogeneous nucleation in α. On the other hand, interstitial (i)-substitutional (s) cluster develops in a bcc α-ferrite matrix, forming coherent plate-shaped precipitates. The solute clustering leads to a significant surface hardening as shown in Figs. 1(a) and (b) [2]. Hardening is more significant than the precipitation of stable B1-type MN due to finer dispersion.

Such monolayer clusters can be formed via two-phase separation in the bcc lattice. Figure 1(c) shows a schematic of the free energy surface of a solid solution in an Fe–M–X ternary system where the free energy was largely stabilized in the high M–X concentration region because of strong attractive X–M interaction. In such a case, there is a strong tendency toward clustering coupled with atomic ordering. The i–s clustering in nitrided steels can be considered similar to the "conditional ordering" or "spinodal ordering" in substitutional alloys, but in complex substitutional and interstitial sublattices. The i–s interactions precisely measured via solubility and internal friction analysis are consistent with clustering behavior observed in experiments [3]. Furthermore, theoretical analysis based on first principles calculation with cluster variation method reveals a clear two-phase separation tendency between Fe and TiN in Fe-Ti-N system. Monte Carlo simulation confirms the planar clustering behavior of Ti and N in the bcc matrix [1].

Strengthening of i-s clustering is also effective in tempering of N martensite or even in the nitriding of fcc-based systems with much larger solubility of interstitial element than bcc lattice. It is also suggested that i-s clustering occurs at migrating interphase boundary, leading to the interphase boundary precipitation, which is used for strengthening of bulk specimen.

As described above, clearly, more attention should be devoted to hidden nanoscale inhomogeneity in "apparent" solid solutions. Sophisticated designs for substitutional and interstitial sublattices should be explored further in the development of new engineering materials.

References

[1] T. Furuhara, Y. Zhang, M. Sato, G. Miyamoto, M. Enoki, H. Ohtani, T. Uesugi, and H. Numakura, Scripta Mater. **223**, 115063 (2023).

[2] G. Miyamoto, Y. Tomio, H. Aota, K. Oh-ishi, K. Hono, and T. Furuhara, Mater. Sci. Technol. **27**, 742 (2011).

[3] G. Miyamoto, H. Numakura, M. Enoki, T. Uesugi, H. Ohtani, and T. Furuhara, Materia Japan **59**, 128 (2020).

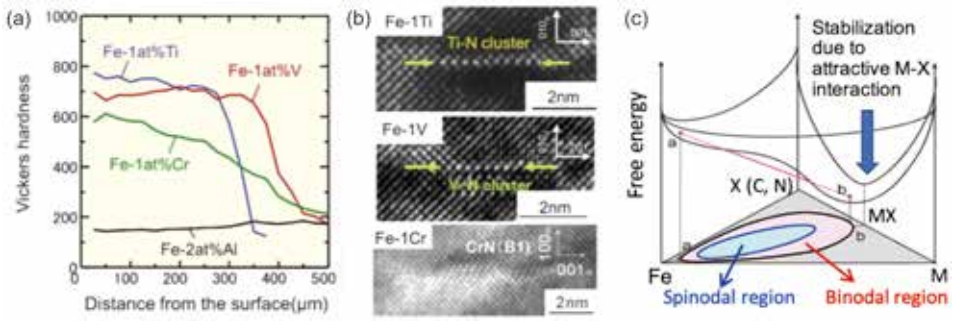

Fig. 1 (a) Hardness profile along the depth direction from the surface of Fe-1at %M binary alloys nitrided at 823 K for 16 h. (b) High-resolution transmission electron micrographs of precipitates in the hardened layer [2], (c) Free energy surface of a solid solution with a tendency toward coupled ordering and phase separation during separation in an Fe–M–X ternary system [1].

Goro Miyamoto (Microstructure Design of Structural Metallic Materials Research Laboratory)
E-mail: goro.miyamoto.e8@tohoku.ac.jp
URL: http://www.st-mat.imr.tohoku.ac.jp/en/index.html

Large-Scale Molecular Dynamics Simulation for High Functional Materials Design and Super-Precise System

To develop high functional and durable materials, an understanding of the multi-physics phenomena, including chemical reaction, friction, stress, fluid, etc. is strongly demanded. We applied reactive molecular dynamics simulation and ab initio calculation to reveal multi-physics phenomena toward the materials design related to mechanical engineering, catalyst, electronic device, and so on.

Development of highly functional and durable materials is vital in many fields. Therefore, deep understanding of multi-physics phenomena including chemical reaction, friction, stress, and fluid etc. are demanded. Recent advances in high-performance computing enable us to simulate the multi-physics phenomena by atomic scale simulations. Therefore, we applied reactive molecular dynamics simulation and ab initio calculation for pioneering next-generation materials design [1-3].

High entropy alloys have showed excellent potential in various applications. However, stress corrosion cracking limits its practical applications. In this work, we conducted tensile simulations for FCC-type $Fe_{40}Ni_{40}Cr_{20}$ alloy to reveal the effects of a high-temperature/pressure water environment on the deformation mechanisms. In a vacuum, we observed the generation of HCP phases during tensile simulation (Fig. 1). While, in the high-temperature/pressure water, the alloy surface was oxidized by chemical reactions with water and this oxide surface layer suppressed the FCC-to-HCP phase transition; instead, a BCC phase was generated (Fig. 1), leading to a reduced ductility because the BCC phase is typically more brittle than FCC and HCP. Thus, the deformation mechanism of the FeNiCr alloy is changed by high-temperature/pressure water [1].

2D transition metal di-chalcogenides have garnered attention in the nonvolatile memory field for their tunable electrical properties. In this study, $NbTe_4$ is identified as a promising candidate with an ultra-low melting point (T_m) and high crystallization temperature (T_c). We showed that the abnormally high resistance caused by the crystallization can be attributed to the reduction of Nb 4*d* orbitals near the Fermi level in collaboration with experimental groups. The simultaneous presence of a low T_m and a high T_c can resolve important issues facing current phase-change memory compounds like poor thermal stability of the amorphous phase [2].

To reveal Co/MFI catalyst structure with higher activity for benzene methylation, we investigated the effects of Al concentrations in Co/MFI on benzene methylation by DFT. Figure 2 shows the energy profile for methane dissociation and benzene methylation on the benzene adsorbed Co ion in Co/MFI with the different Al concentrations. Here,

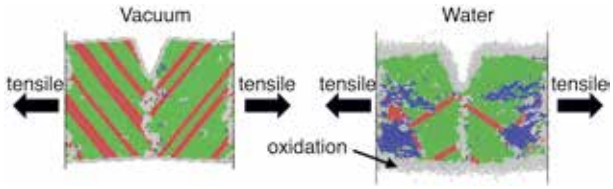

Fig. 1 Tensile simulation results in vacuum (left) and high-temperature/pressure water. Green, red, blue, and gray indicate the FCC, HCP, BCC and other structure, respectively.

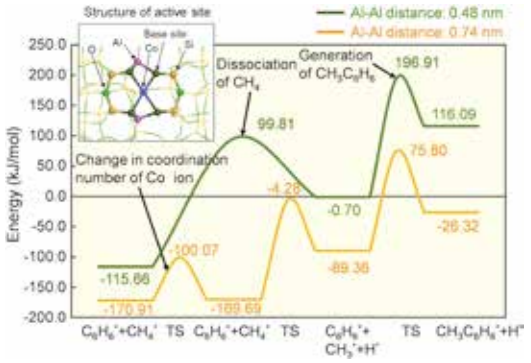

Fig. 2 The energy profile for methane dissociation and benzene methylation in Co/MFI with the different Al–Al distances.

the higher the Al concentration, the closer the distance between Al atoms. The energy profile shows that CH_3–C_6H_6 formation is the rate-determining step, and the calculated apparent activation energies with 0.48 and 0.74 nm of the Al–Al distance are 196.91 kJ/mol and 75.80 kJ/mol, respectively. The experimental apparent activation energy (110 kJ/mol) is near the calculation value in the Co/MFI with 0.74 nm of the Al–Al distance. Thus, Co/MFI with lower Al concentration is effective for high activity for benzene methylation [3].

References

[1] Y. Wang, H. Zhao, C. Liu, Y. Ootani, N. Ozawa, and M. Kubo, RSC Adv. **13**, 6630 (2023).

[2] Y. Shuang, Q. Chen, M. Kim, Y. Wang, Y. Saito, S. Hatayama, P. Fons, D. Ando, M. Kubo, and Y. Sutou, Adv. Mater. **35**, 2303646 (2023).

[3] N. Katada, N. Ozawa, E. Tsuji, K. Kanehara, A. Otsuka, T. Sakamoto, K. Umezawa, H. Matubara, S. Suganuma, and M. Kubo, Microporous Mesoporous Mater. **364**, 112855 (2024).

Momoji Kubo (Materials Design by Computer Simulation Research Laobratory)
E-mail: momoji@tohoku.ac.jp
URL: https://www.simulation.imr.tohoku.ac.jp/eng/index.html

Environment-Assisted Cracking of Magnesium Alloy in Aqueous Solution Under Various Potentials

Magnesium alloys suffered from environment-assisted cracking under stress in corrosive environments. In this study, we investigated the effect of potentials on the environment-assisted cracking behavior of a magnesium alloy. Slow strain tensile tests in an aqueous solution under various potentials revealed that environment-assisted cracking of the magnesium alloy became more severe under relatively high potential owing to corrosion accompanied by enhanced hydrogen absorption.

Magnesium alloys are expected to achieve practical usages for transportation applications because of their relatively high strength-to-weight ratio. However, it is known that environment-assisted cracking (EAC) occurs when magnesium alloys are used under stress in corrosive environments. The main mechanism of EAC for magnesium alloys is considered to be hydrogen embrittlement, which is caused by hydrogen absorbed into the material. On the other hand, the EAC of magnesium alloys tends to occur at relatively noble potentials in an aqueous solution, where hydrogen evolution reaction is relatively slow, and the amount of hydrogen absorbed into magnesium alloys is expected to be small. Thus, there are many remaining unclear details of the EAC mechanism of magnesium alloys. In this study, slow strain rate tensile tests of a magnesium alloy (Mg-3Al-1Zn by wt.%) were conducted in an aqueous solution to clarify the effects of anodic magnesium dissolution and hydrogen evolution reactions on the EAC behavior of the magnesium alloy [1]. The rates of hydrogen evolution and magnesium dissolution reactions were varied by changing the polarization potential of the magnesium alloy.

Figure 1 shows engineering stress-strain curves of magnesium alloy tested in various environments. The mechanical properties of the magnesium alloy considerably degraded in the aqueous solution compared to that in air. The total elongation became smaller, and the flow stress decreased with the positive shift in cathodic potential. From the surface and cross-sectional observations after tensile testing, the corrosion reaction occurred more severely with the positive shift in cathodic potential and many cracks were observed on the surface. The amount of absorbed hydrogen in the magnesium alloy was measured after the tensile testing. The estimated hydrogen absorption rates increased with the positive shift in cathodic potential although the rate of hydrogen evolution reaction decreased (Fig. 2). This result indicates that hydrogen absorption may be enhanced by the formation of a fresh surface

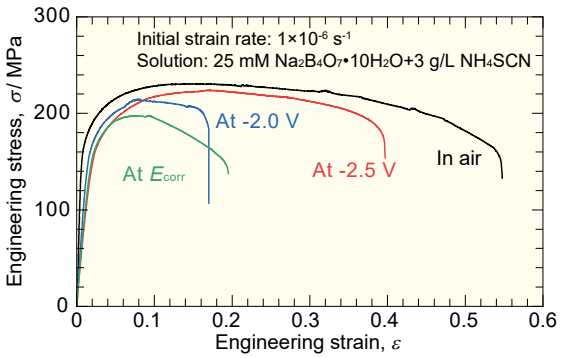

Fig. 1 Engineering stress-strain curves of magnesium alloy tested in various environments with an initial strain rate of 1 x 10^{-6} s^{-1}. E_{corr} represents corrosion potential [1].

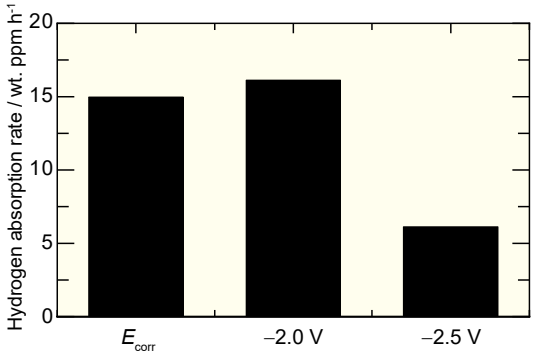

Fig. 2 Average hydrogen absorption rates of magnesium alloys calculated with the hydrogen content and the time to fracture [1].

via magnesium dissolution reaction, which is enhanced by the potential shift in the positive direction.

This study clarified that the mechanical properties of magnesium alloys degraded more severely under relatively high potential owing to magnesium dissolution accompanied by enhanced hydrogen absorption.

References

[1] S. Ajito, T. Hojo, M. Koyama, S. Hiromoto, and E. Akiyama, Corros. Sci. **218**, 111195 (2023).

Saya Ajito (Environmentally Robust Materials Research Laboratory)
E-mail: saya.ajito.d1@tohoku.ac.jp
URL: http://akiyamaimr-e.amebaownd.com/

Suzuki Segregation in High-Entropy Alloys

Determining elemental segregation at stacking faults (SFs), i.e., Suzuki segregation, has been a longstanding issue in concentrated solid-solution alloys, drawing attention from both the scientific and industrial communities. With the aid of scanning transmission electron microscopy (STEM) techniques, we successfully captured a trace of Suzuki segregation in a solid solution of high-entropy alloys (HEAs)

The segregation of alloying elements into lattice defects plays a crucial role in determining the mechanical properties of structural alloys. Suzuki segregation, involving chemical interactions between alloying elements and SFs, serves as a vital strengthening mechanism, especially for concentrated face-centered cubic solid-solution alloys with low stacking fault energy (SFE). Traditionally, Suzuki segregation and the resulting hardening have been employed in commercialized Co–Ni–Cr–Mo alloys, developed through an industry-IMR collaboration [1]. These alloys are utilized as precision springs in mechanical watches and medical devices. Previous studies have further highlighted its significant role in Ni-base superalloys and Mg alloys, particularly in their high-temperature deformation behaviors. However, unlike those in an ordered structure, direct observation of Suzuki segregation in solid solutions remains challenging due to the relatively low segregation concentration and the presence of severely distorted matrices.

In this study [2], we characterized Suzuki segregation in HEAs—a new class of multiprincipal element alloys. A $Co_{0.95}Cr_{0.8}Fe_{0.25}Ni_{1.8}Mo_{0.475}$ HEA, designed to contain a large amount of Mo (~11 at.%) [3], was processed by heavy cold-rolling (CR) and subsequently aged at 773 K. The alloy's strength exhibited a significant improvement after strain aging, reaching 2.1 GPa. High-angle annular dark-field (HAADF) STEM imaging, coupled with corresponding energy-dispersive X-ray spectroscopy (EDS) elemental analysis, was performed on a sample carefully prepared with a focused ion beam system. Aligning the [110] crystallographic orientation of the sample with viewing direction was preferable for subsequent STEM-EDS analysis. Elemental mapping successfully captured traces of Co enrichment at SFs, demonstrating the pinning of Shockley partial dislocations via segregated atoms during strain aging. Interestingly, co-segregation of Co and Mo atoms at SFs was otherwise observed in a strain-aged specimen with a small pre-strain (Fig. 1). This highlights that the amount of pre-straining, dominating the density of SFs, alters the segregation tendency in the same alloy. The local SFE with the segregation of Co and Mo atoms was −30.6 mJ/m^2 at the aging temperature, as calculated via a phase-field method. The negative SFE indicates the stabilization of SFs through segregation, leading to the formation of wide SFs. The obtained results enhance our fundamental understanding of Suzuki segregation and will contribute to the design of high-strength alloys.

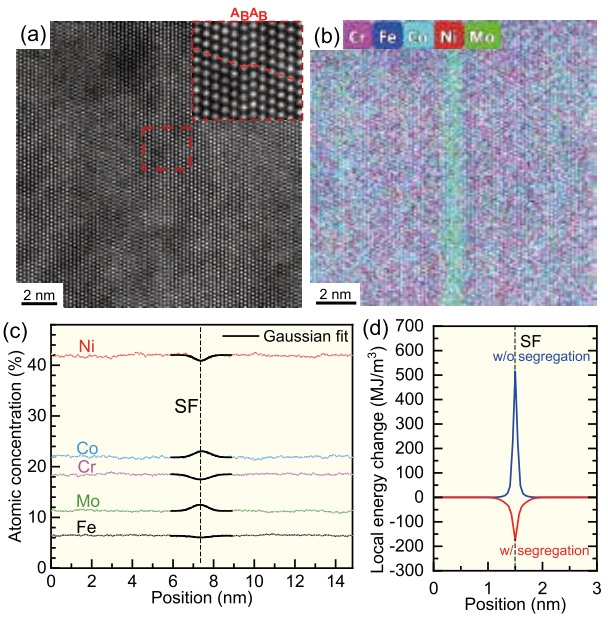

Fig. 1 (a) HAADF-STEM image, (b) STEM-EDS map, and (c) line profile of the aged specimen. (c) Calculated local energy change profile across the SF.

References

[1] A. Chiba and M. Kim, Mater. Trans. **42**, 2112 (2001).

[2] J. Li, K. Yamanaka, Y. Hayasaka, and A. Chiba, Scr. Mater. **226**, 115226 (2023).

[3] J. Li, K. Yamanaka, and A. Chiba, Mater. Sci. Eng. A **817**, 141359 (2021).

Kenta Yamanaka (Deformation Processing Research Laboratory)
E-mail: kenta.yamanaka.c5@tohoku.ac.jp
URL: http://www.imr.tohoku.ac.jp/en/about/divisions-and-centers/research-division/24.html

International Co-Authored Paper

Enhancement of Grain-Boundary Strength by Elemental Doping in Magnesium-Aluminate Spinel

In order to improve mechanical properties in polycrystalline magnesium-aluminate spinel material, earth-abundant Y element was doped. Hardness and fracture toughness were slightly improved in a Y-doped specimen. Using advanced electron microscopy and spectrometry techniques, it was confirmed that doped Y atoms were preferentially segregated at the grain boundary by substituting Al atoms at octahedral sites. Furthermore, those Al atoms removed from the octahedral sites at the grain-boundary occupy the tetrahedral Mg sites in the vicinity of the grain boundary.

Magnesium aluminate spinel (MAS, $MgAl_2O_4$) is a unique ceramic material that is transparent over a wide range from ultraviolet to mid-infrared with enhanced toughness, which could be utilized for windows in extreme environments, e.g. at higher temperatures. However, fracture failures tend to occur at grain boundaries (GBs), which is one of the major limiting factors for practical MAS applications. Mechanical properties at GBs can be improved by doping certain elements through modifying atomic arrangements at GBs in MAS. In this study, earth-abundant Y was doped to polycrystalline MAS to improve mechanical properties such as fracture toughness.

It was confirmed that mechanical properties with respect to the hardness and fracture toughness in the Y-doped MAS were slightly improved in comparison to the pristine pure MAS. In addition, microstructure and chemistry in the vicinity of GBs of the Y-doped MAS were examined by aberration-corrected scanning transmission electron microscopy (STEM) with electron energy-loss spectrometry (EELS) analysis. Figure 1 shows an atomic resolution high-angle annular dark-field (HAADF) image at a GB in the Y-doped MAS [1]. The brighter regions indicate heavy atomic-number Y atoms in this imaging mode. So that, the doped Y atoms are segregated at the GB. And it was confirmed that Y atoms occupy octahedral Al sites. Figure 2 shows a series of composition maps with a HAADF-STEM image (a) at a GB in the Y-doped MAS, quantified by EELS analysis in aberration-corrected STEM. The Y segregations along the GB were confirmed both through the HAADF-STEM image (Fig. 2a) and the quantified Y map (Fig. 2b). In addition to Y segregation, Al is also segregated in the vicinity of the GB rather broadly whereas the Mg concentration is depleted at the GB. Based on the quantified compositional maps of these elements, it can be estimated that rather complicated atomic rearrangement occurred at the GB: doped Y atoms substitute Al atoms at the GB, then the removed Al atoms from the GB occupied the Mg tetrahedral sites subsequently. It was never possible to find out such complicated segregation behaviors at the GB without applying appropriate quantitative analysis [2].

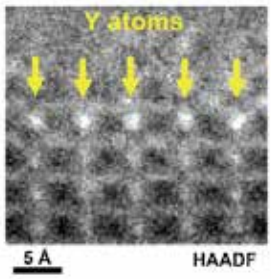

Fig. 1 An atomic-resolution HAADF-STEM image of a GB in Y-doped MAS.

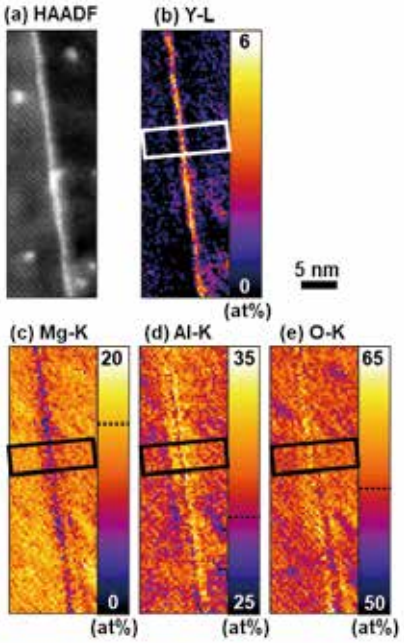

Fig. 2 A HAADF-STEM image (a) with a series of composition maps: (b) Y, (c) Mg, (d) Al, and (e) O, quantified by EELS analysis.

References

[1] A. Campos-Quiros, A. Kundu, and M. Watanabe, Microsc. Microanal. **29**, Suppl. 1, 407 (2023).

[2] M. Watanabe, G. Guzzinati, P. Kükelhan, V. Gerheim, M. Linck, H. Müller, M. Haider, T. F. Hoffman, T. Isabell, N. Shimura, and H. Sawada, Microsc. Microanal. **29**, Suppl. 1, 416 (2023).

Masashi Watanabe (Analytical Science Research Laboratory)
E-mail: masashi.watanabe.d2@tohoku.ac.jp
URL: http://www.imr.tohoku.ac.jp/en/about/divisions-and-centers/research-division/27.html

Reactive Oxygen Species Generation on Nitrogen-Doped Titanium Under Visible Light Irradiation

Pure titanium and titanium alloys such as Ti-6Al-4V are commonly used as biomaterials because of their good biocompatibility and high corrosion resistance. In this study, Nitrogen-doped TiO_2 (N-doped TiO_2) was formed on a Ti substrate, and reactive oxygen species resulting from the visible light-induced photocatalytic activity of the N-doped TiO_2 was investigated.

Titanium dioxide (TiO_2) forms on surfaces of titanium (Ti), and this titanium oxide layer is responsible for the biocompatibility. Numerous studies have reported that anatase-type TiO_2 exhibits high photocatalytic activity; when it is irradiated with ultraviolet light, it reacts with water or O_2 surrounding it and generates reactive oxygen species (ROS). In addition, hydrogen peroxide and hydroxyl radicals are known to be generated as ROS on TiO_2 photocatalysts. N-doped TiO_2 also exhibits visible light-induced photocatalytic activity. N-doped TiO_2 subjected to NaOH and hot water and heated in an ammonia gas atmosphere showed visible light-induced antimicrobial activity and biocalcification ability [1,2]. On the other hand, as a related study, we also conducted a study on Ag and Cu co-doped TiO_2 prepared by the chemical and thermal treatment of Ti metal [3].

The objective of this study is to investigate the ROS generated via visible light-induced photocatalytic activity on N-doped TiO_2.

To prepare N-doped TiO_2, we polished commercial-grade pure Ti (cp Ti) plates and soaked them in NaOH solution and hot water. These plates were subsequently heated at 500 °C for 3 h under an ammonia gas atmosphere in a tubular electric furnace.

Figure 1 shows the generated amount of hydroxyl radicals for each sample, which was 0.290 μM for the cp Ti and 0.825 μM for the N-doped TiO_2 plate (500-3 h). The results show that more hydroxyl radicals were generated with a N-doped TiO_2 plate than with a cp Ti plate.

Figure 2 presents measurement results of the concentration of hydrogen peroxide generated in purified water, each of which carried a sample of cp Ti or N-doped TiO_2 (500-3 h), and each of which was subjected to visible light irradiation for 15 min. The concentration of hydrogen peroxide generated in the purified water with cp Ti irradiated with visible light for 15 min was 0.31 μM, whereas that with N-doped TiO_2 (500-3 h) was 1.16 μM.

N-doped TiO_2 prepared in this study exhibited photocatalytic activity under visible light irradiation,

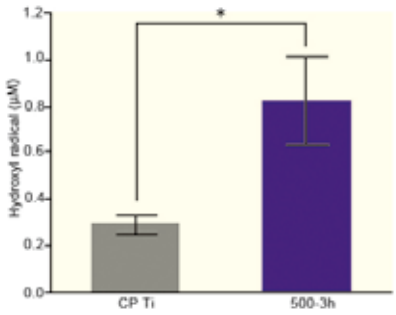

Fig. 1 Electron-spin resonance spectra under visible-light irradiation of (a) cp Ti and (b) N-doped Ti plate (500-3 h). Asterisk (*) represents a significant difference at $p < 0.05$

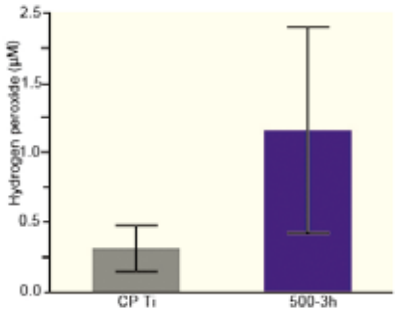

Fig. 2 Generated amount of hydrogen peroxide on cp Ti and N-doped TiO_2 (500-3 h) under visible light irradiation (all data are expressed as the average± SD; n = 3)

were generated hydroxyl radical and hydrogen peroxide. The results suggested that ROS generated by the photocatalytic reaction.

References

[1] M. Kawashita, N. Endo, T. Watanabe, T. Miyazaki, M. Furuya, K. Yokota, Y. Abiko, H. Kanetaka, and N. Takahashi, Colloids Surf. B: Biointerfaces **145**, 285 (2016).

[2] M. Iwatsu, H. Kanetaka, T. Mokudai, T. Ogawa, M. Kawashita, and K. Sasaki, J. Biomed. Mater, Res. B: Applied Biomaterials **108(2)**, 451 (2020).

[3] K. Suzuki, M. Iwatsu, T. Mokudai, H. Kanetaka, M. Shimabukuro, T. Yokoi, and M. Kawashita, Molecules **28(2)**, 650 (2023).

Takayuki Mokudai (Design & Engineering by Joint Inverse Innovation for Materials Architecture)
E-mail: tmokudai@tohoku.ac.jp
Hidemi Kato (Project Leader of Design & Engineering by Joint Inverse Innovation for Materials Architecture)
E-mail: hidemi.kato.b7@tohoku.ac.jp
URL: http://www.imr.tohoku.ac.jp/en/about/divisions-and-centers/research-division/29.html

Energy-Related Materials

IMR KINKEN Research Highlights 2024

GIMRT International Co-Authored Paper

Growth Kinetics of {100} and {110} Crystal-Melt Interfaces of Silicon

Dynamics of crystal-melt interface on the rough {100} and {110} planes of silicon were investigated by in situ observation experiments. It was clearly shown that both growth velocities are similar, and the ratio of the kinetic coefficients of both planes are comparable.

Anisotropy of the growth velocity is the most fundamental issue in crystal growth, and the growth velocity of silicon is well known to be anisotropic, depending on the growth crystallographic orientation. In general, when the driving force ($\Delta\mu$) for crystal growth is small, the growth velocity (V) is expressed with a kinetic coefficient β as $V \approx \beta \cdot (\Delta\mu/kT)$, where k is the Boltzmann's constant and T is an absolute temperature. Since the incorporation of atoms into the crystal surface at the crystal-melt interface is greatly affected by the atomic smoothness of the crystal surface, the value of β is different for each crystallographic plane. However, the literature contains limited reports on the anisotropy of growth velocities of rough interfaces with different orientations. That is, the difference in growth kinetics between {100} and {110} interfaces, for example, is not yet fully known. Therefore, in this study, in situ experiments are performed in order to clarify the difference in growth velocities (i.e., kinetic coefficients) for the crystal-melt interfaces with <100> and <110> rough growth directions [1].

An in situ observation system was used to observe and record the crystal-melt interface with <100> and <110> orientations during the unidirectional solidification process. Two silicon wafers having a crystallographic orientation of <100> and <110> in the growth direction were placed side by side in a silica crucible. The wafers were carefully melted from one side and heating was stopped to create a state in which the remaining crystals (seed crystals) and melt are in equilibrium. The sample was then cooled to initiate crystal growth from the seed crystals. Experiments were performed at three cooling rates: 3 K·min^{-1}, 10 K·min^{-1} and 40 K·min^{-1} , and the solidification processes were recorded using a high-speed thermal camera and the recorded video was analyzed.

Figure 1 shows (a) the crystal-melt interface of crystals growing in the <100> and <110> directions, and (b) the growth velocity change of both interfaces obtained from the video analysis [1]. It can be seen that the growth velocities of both interfaces are comparable. Similar results were obtained for all samples.

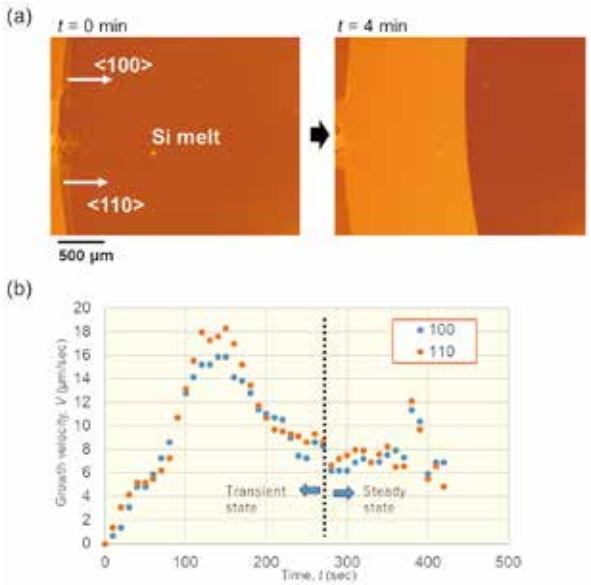

Fig. 1 (a) Snapshots of unidirectional solidification process at a cooling rate of 3 K·min^{-1}. (b) Plot of growth velocity as function of time for {100} and {110} interfaces [1].

From the microstructural analysis of the post-solidification sample, the direction of grain boundary movement during steady-state growth was measured, and from that result and Equation (1), the ratio of kinetic coefficient for growth in the <100> and <110> directions was obtained.

$$\phi = \frac{\pi}{2} - \sin^{-1}\frac{K(100)}{K(110)} \quad , \quad (1)$$

where ϕ is the grain boundary angle to the growth direction and $K(100)$ and $K(110)$ are kinetic coefficients for (100) and (110) planes, respectively. It was found the ratio of both kinetic coefficients, $K(110)/K(100) = 1.05$. In this way, it is experimentally confirmed that the kinetic coefficients for the {100} and {110} crystal-melt interfaces are similar, within a 5% accuracy.

References

[1] S. S. Mishra, L.-C. Chang, K. Maeda, J. Nozawa, H. Morito, T. Duffar, and K. Fujiwara, J. Crystal Growth **627**, 127524 (2024).

Kozo Fujiwara (Crystal Physics Research Laboratory)
E-mail: kozo.fujiwara.c6@tohoku.ac.jp
URL: http://www.imr.tohoku.ac.jp/en/about/divisions-and-centers/research-division/02.html

GIMRT

Direct Observation of Voids Decorated with Transmuted Rhenium Atoms in Neutron-irradiated Tungsten by Transmission Electron Microscopy and Atom Probe Tomography

Radiation damage in tungsten which is a candidate material for the plasma-facing components of fusion reactors was investigated by both transmission electron microscopy and atom probe tomography. Voids decorated with transmuted rhenium atoms in (initially pure) tungsten neutron-irradiated in the fast-neutron experimental reactor Joyo were clearly observed, which contribute to understanding the formation mechanism of the irradiation-induced defects.

Tungsten (W) is a candidate material for the plasma-facing components of fusion reactors. Plasma-facing materials are exposed to an intense neutron-irradiation field during fusion reactor operation. Neutron-irradiation of W causes degradation of its mechanical and thermal properties, which is due to the formation of irradiation-induced defect clusters (e.g., voids and dislocation loops) by displacement damage, such as vacancies and self-interstitial atoms, and the formation of irradiation-induced clusters or precipitates by solid transmutation elements such as rhenium (Re) and osmium (Os) in W. Therefore, it is important to understand microstructural changes in W caused by the irradiation [1].

Transmission electron microscopy (TEM) can reveal the structure of defects formed by neutron-irradiation, but it is difficult to observe compositional changes due to nuclear transmutation. On the other hand, atom probe tomography (APT) cannot obtain information about the defect structure, but can detect the compositional changes. In the present study, we applied correlative microscopy using TEM and APT to (initially pure) W neutron-irradiated up to 1.54 dpa at 750 ˚C in the fast-neutron experimental reactor Joyo where the thermal neutron ratio is low, and investigated the structure and chemistry of the defects formed by neutron- irradiation [2].

Figure 1 shows a TEM image and an APT map for Re obtained from the same area of the needle specimen. Voids with a high number density were clearly observed in the TEM image, which was taken in an under-focused condition to emphasize the voids. Re-enriched clusters were observed in the APT map. It should be noted that APT cannot obtain an elemental map of the whole needle specimen, but only the central part. By comparing the TEM image and the APT map, a one-to-one correspondence was clearly obtained between the voids in the TEM image and the Re-enriched clusters in the APT map. It was found that the voids and the Re-enriched clusters do not exist independently but are present at the same position. The size distribution for the Re-enriched clusters is almost the same as that for the voids. The above results show that all voids are decorated with transmuted Re atoms in the (initially pure) W neutron-irradiated in Joyo where the thermal neutron ratio is low, and that no Re-enriched clusters or Re-precipitates are unrelated to voids.

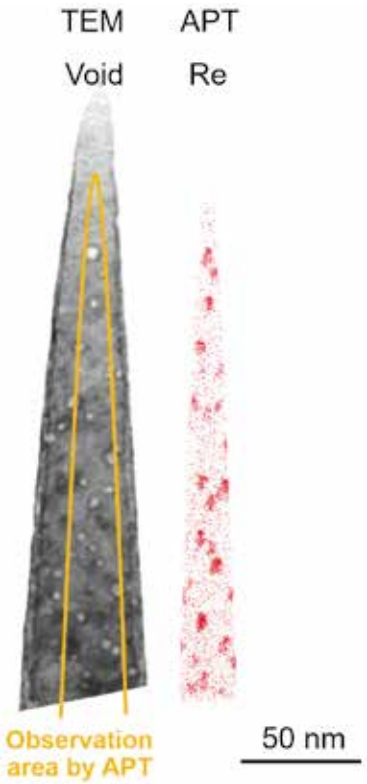

Fig. 1 TEM image and APT map for Re obtained from the same needle specimen of (initially pure) W neutron-irradiated in the fast-neutron experimental reactor Joyo. A one-to-one correspondence was clearly obtained between the voids in the TEM image and the Re-enriched clusters in the APT map.

References

[1] Y. Hatano, J. Wang, T. Toyama, T. Hinoki, K. Yabuuchi, Y. Zhang, B. Ma, A. V. Spitsyn, N. P. Bobyr, K. Inoue, and Y. Nagai, Materials & Design **229**, 111899 (2023).

[2] K. Inoue, T. Yamashita, S. Nogami, A. Hasegawa, T. Toyama, and Y. Nagai, Materialia **32**, 101963 (2023).

Yasuyoshi Nagai and Koji Inoue (Irradiation Effects in Nuclear and Their Related Materials Research Laboratory)
E-mail: koji.inoue.e2@tohoku.ac.jp
URL: http://www.imr.tohoku.ac.jp/en/about/divisions-and-centers/research-division/11.html

Volumetric Change of SiC Under Irradiation

Silicon carbide (SiC) fiber-reinforced matrix composite (SiCf/SiC) is a candidate material for advanced fusion reactor blankets. We clarified the volumetric change of SiC due to irradiation and its effect to the mechanical properties using ultra-small testing technologies (USTT). Furthermore, we utilized the USTTs for evaluating the interfacial mechanical strength of tungsten-coated ferritic steel for fusion reactors.

Materials resistant to extreme environments such as oxide dispersion strengthened (ODS) alloys [1], ceramics [2-4] and heavy alloys [5] are crucial for realizing advanced nuclear systems, such as Gen IV fission reactors and fusion reactors.

Silicon carbide (SiC) fiber-reinforced matrix composite (SiCf/SiC) is a candidate ceramic material for fusion reactor blankets because of its high-temperature environmental resistance, low activation properties, and irradiation resistance. This study investigated the effect of annealing temperature on the proportion of shrinkage and swelling of SiC fiber in SiCf/SiC irradiated at 30 °C to 100 dpa by Si-ion beam [2]. After the irradiation, the compressive displacement of > 60% of the fibers before failure increased to more than 1.5 times that of the as-received specimen. Significant swelling indicates that the proportion of swelling was higher than that of shrinkage after irradiation. This can be attributed to the amorphization of SiC, and its amorphization threshold dose increased with decreasing grain boundary volume fraction. These findings provide insights into the mechanism of irradiation-induced fiber amorphization of SiC. In order to obtain high-strength TiB-TiB_2 ceramics by low-temperature sintering, a new mechanically milled sintering aids was also developed [3].

In fusion reactors, plasma facing components need high-temperature stability, resistance to surface sputtering, low-retention of tritium and irradiation resistance. Vacuum plasma spray (VPS) coating is a prospective technology for the fabrication of tungsten-coated reduced activation ferritic steel (W-RAF steel). However, detailed evaluation on the mechanical properties of W-RAF steel joints has been limited because of the thin coating layer. In this study [5], the mechanical properties of the W coating and W–RAF steel interface were evaluated using double-notched micropillar compression tests. The ultimate shear strength of the interface area exhibited a similar to that of the W layer and higher than that of the RAF steel (F82H) substrate, as shown in Fig. 2. The fracture microstructure elucidated the importance of improving the mass densities of W coatings to improve the mechanical performance of vacuum-plasma-sprayed W–steel joints. Effective bonding of a W/F82H interface and the adjacent RAF steel substrate via VPS results in high strength and ductility of the interface area, and hence the W-RAF steel joint, against shearing and bending loads.

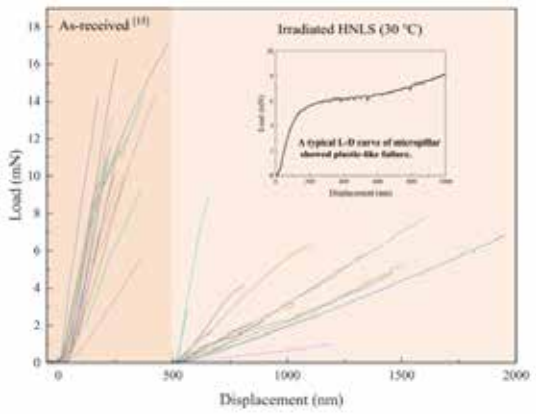

Fig. 1 Load–displacement curves of the two types of fibers [2].

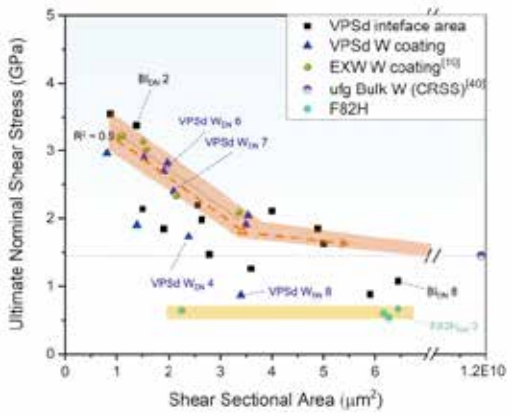

Fig. 2 Ultimate nominal shear stress versus shear sectional area of the tested DNS samples [5].

References

[1] H. Yu, S. Kondo, R. Kasada, and S. Ukai, Corr. Sci. **212**, 110933 (2023).

[2] X. Yuan, S. Kondo, K. Yabuuchi, H. Yu, Y. Ogino, and R. Kasada, J. Eur. Ceram. Soc. **43**, 5125 (2023).

[3] Y. Jimba, Y. Okuno, S. Kondo, H. Yu, Y. Ogino, S. Nogami, and R. Kasada, Ceram. Int. **49**, 34863 (2023).

[4] S. Iwamoto, S. Kondo, H. Katsui, K. Shimoda, H. Yu, Y. Ogino, and R. Kasada, Int. J. Appl. Ceram. Technol., 1-9 (2023) in press.

[5] X. Wu, S. Kondo, H. Yu, T. Nagasaka, and R. Kasada, Surf. Coat. Technol. **462**, 129468 (2023).

Ryuta Kasada, Sosuke Kondo, Hao Yu, and Yasuyuki Ogino (Nuclear Materials Engineering Research Laboratory)
E-mail: ryuta.kasada.e7@tohoku.ac.jp
URL: http://www.imr.tohoku.ac.jp/en/about/divisions-and-centers/research-division/13.html

Beyond Tantalum and Tungsten: The Rise of Single-Crystal Alloys in Resistance Heating

We have developed single-crystal alloy wires using the crystal growth method, which has resulted in a breakthrough in resistance heating wires. The new alloy wires offer improved workability, high-temperature durability, and lower power consumption, overcoming the limitations of traditional Ta and W wires. This innovation opens up previously unattainable alloy systems, promising new industrial applications.

Around 20 years after Edison's invention of using bamboo as a filament for incandescent lamps in 1883, it was discovered that tantalum (Ta) could also be used as a metal filament. However, despite its excellent ductility, Ta wire was soon replaced by tungsten (W) filaments due to the disadvantage of deterioration caused by grain growth. Although incandescent lamps have been replaced by newer technologies such as fluorescent lamps, LEDs, and organic ELs, refractory metals such as W, Mo, and Ta have been used as high-temperature metal resistance heating elements for over 100 years.

An important application of resistance heating wire is in vacuum deposition cells, which are also used for organic EL deposition. The Ta wire commonly used in these cells gradually forms a nodular structure and deteriorates with use, requiring replacement approximately every 1,000 hrs. Therefore, due to the increasing use of organic EL in recent years, there is a demand for a new resistance heating wire that is more durable, consumes less power, and is easy to process at room temperature.

We addressed this problem by considering the possibility of expanding the range of material selection by single-crystallizing the wire to essentially eliminate intergranular cracking and provide workability. The micro-pulling-down method (μ-PD method) is a fast and effective way to fabricate single crystals several centimeters in size. However, it was originally designed only for screening purposes. To replace the current plastic forming method with the μ-PD method, certain challenges had to be overcome: the method had to be capable of producing tens of meters or more of wire per day with an accuracy of ϕ0.8 mm ±12 μm or less, and it had to have no casting defects inside or on the surface of the wire.

Through the analysis of the μ-PD method, we found that excellent shape controllability can be achieved under certain wetting conditions, and we also found conditions that allow crystal growth at several hundred mm/min, which is several tens of times faster than conventional methods [1,2].

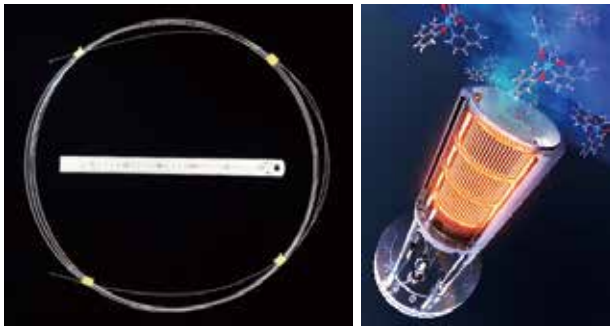

Fig. 1(a) shows the grown wire of Ruscaloy and (b) shows the image of deposition cell.

Additionally, we developed Ruscaloy, a novel alloy suitable for this method, and successfully fabricated a deposition cell to perform organic EL film deposition [3]. This alloy exhibited excellent properties such as flexibility and strength (εrp=~80%, σTS=~550MPa) that can be easily processed at room temperature, and exhibits more than 3 times higher temperature durability (>3000h@1600°C), 10% lower power consumption, and 2 times faster return to deposition rate compared to conventional Ta wire.

Our results shed new light on alloys that were previously unusable due to workability issues with the crystal growth method. We also demonstrated new possibilities for traditional materials like resistance heating wire. There is still much to be explored, not only in terms of alloy properties, but also in terms of the physics of crystal growth, which is of inexhaustible interest.

References

[1] R. Murakami, K. Oikawa, K. Kamada, and A. Yoshikawa, ACS Omega **6**, 8131 (2021).

[2] R. Murakami, K. Oikawa, K. Kamada, S. Itoi, and A. Yoshikawa, J. Cryst. Growth **629**, 127565 (2023).

[3] R. Murakami, K. Kamada, K. Umetsu, T. Yoshioka, K. Oikawa, J. Kido, and A. Yoshikawa, Int. J. Refract. Met. Hard Mater. **114**, 106235 (2023).

Rikito Murakami (Advanced Crystal Engineering Research Laboratory)
E-mail: rikito.murakami.d4@tohoku.ac.jp
URL: http://yoshikawa-lab.imr.tohoku.ac.jp/index-e.html

Larger Amounts of Water Intercalation into Heat-Storage Layered MnO_2 Induced by Interlayer-Cation Disorder

Layered manganese dioxide containing K cations and water molecules in between the MnO_2 layers exhibits reversible heat storage properties via a water-intercalation mechanism with a certain amount of an irreversible capacity of water intercalation after the initial thermal cycle. We have elucidated that the irreversibility originates in the occupation behavior of the interlayer K cations that compete for the most stable sites with excess water molecules existing in the as-synthesized state.

Heat storage materials can store waste heat and release the thermal energy on demands. Among those materials, a K-containing layered manganese dioxide ($K_{0.33}MnO_2{\cdot}0.83H_2O$) has been found to exhibit excellent heat-storage properties, including high environmental integrity, high thermal energy density, fast charge/discharge rates, and good cyclability, owing to a water-intercalation mechanism [1]. The K-containing MnO_2 can reversibly absorb and release 0.50 mol molecules per MnO_2 resulting in a reversible thermal energy density exceeding 1,000 MJ/m^3. However, it exhibits irreversible capacity of water intercalation (0.33 mol per MnO_2) in the initial heating/cooling cycle, which limits the reversibly available energy density of the material for the subsequent cycles.

To elucidate the origin of the initial irreversible capacity, we investigated the crystal structure of the layered manganese dioxide in the as-synthesize and heat-treated states by atomic-resolution scanning transmission electron microscopy (STEM) [2,3]. The interlayer K cations in the as-synthesized state are randomly arranged in some of the interlayers (open yellow arrows in Fig. 1(a)) because excess water molecules prevent the K cations from occupying the most stable interlayer site (Wyckoff 2*c* site in space group $P6_3/mmc$). After heat treatment at 250°C, on the other hand, the interlayer K cations occupy every third 2*c* site in all the interlayers, showing a tripled periodicity along the *a*-axis direction (solid yellow arrows in Fig. 1(b)). This infers that simultaneous occupancy at the 2*c* site of the K cation and the water molecules cannot be realized, and the heat treatment allows the K cation to move from its metastable position to the most stable position (2*c* site) in the absence of water molecules at high temperatures. This competitive occupancy is schematically illustrated in Fig. 1(c). To minimize the irreversible capacity of water intercalation, and hence, to increase the thermal energy density, replacing interlayer K cations with other species and/or optimizing the content of interlayer cations that change the interaction between the interlayer cations and water molecules will be effective.

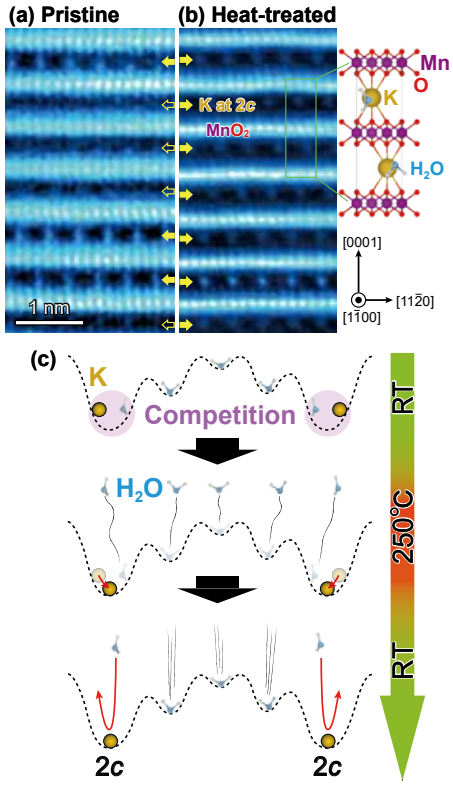

Fig. 1 STEM images of (a) pristine and (b) heat-treated K-containing MnO_2 taken along the *a*-axis direction. (c) Schematic illustrations of potential energy surfaces for the interlayer K cations and water molecules during the first release/absorption of water molecules from/to $K_{0.33}MnO_2$.

References

[1] T. Hatakeyama, N. L. Okamoto, S. Otake, H. Sato, H. Li, and T. Ichitsubo, Nat. Commun. **13**, 1452 (2022).
[2] N. L. Okamoto, H. Yoshisako, and T. Ichitsubo, Energy Stor. Mater. **61**, 102912 (2023).
[3] N. L. Okamoto, H. Yoshisako, and T. Ichitsubo, J. Phys. Chem. C **127**, 20956 (2023).

Norihiko L. Okamoto and Tetsu Ichitsubo (Structure-Controlled Functional Materials Research Laboratory)
E-mail: nlokamoto@tohoku.ac.jp, tichi@tohoku.ac.jp
URL: http://ilab.imr.tohoku.ac.jp/

International Co-Authored Paper

Partial Liquid Metal Dealloying to Synthesize Nickel-Containing Porous Ferrous and High-Entropy Alloys

Liquid metal dealloying is a promising technique to produce bicontinuous porous metals with high specific surface areas. However, it has not been applied to produce nickel-containing porous metals because of the lack of a suitable metallic bath. Here we show that nickel-containing porous and composite metals can be produced by partial liquid metal dealloying.

Nanoporous metals with bicontinuous microstructures are attracting increasing attention owing to their outstanding performance. Such nanoporous materials are prepared by the selective removal of a component from a solid alloy, also known as dealloying. Dealloying was initially introduced as an electrochemical process whereby the less-noble component of the precursor selectively dissolves into an aqueous solution, whereas the remaining noble component self-organizes into a three-dimensional nanoporous structure. However, this electrochemical technique is only applicable to elaborate nanoporous structures comprising noble metals.

Liquid metal dealloying (LMD) has emerged as a versatile method that can be used to produce porous and composite metals with various elements [1]. In LMD, the selective dissolution is driven by the mixing enthalpy between species. Let us consider a generic A-B precursor alloy immersed in a liquid metal C. Selective dissolution of B and formation of nanoporous A, as shown in Fig.1(a), occurs if A is immiscible in C ($\Delta H_{mix}^{A\text{-}C}$ large) and B is miscible in C ($\Delta H_{mix}^{B\text{-}C} \lesssim 0$). Using LMD, porous and composite materials comprising less-noble metals and alloys have been successfully fabricated. These materials present advantageous functional properties for battery electrodes, electrolytic capacitors, and catalytic materials. In the previous LMD studies, Mg, Cu, and Bi are commonly used in the metallic baths, however, the high miscibility of Ni in these liquids precludes the application of LMD to the production of Ni-containing porous alloys, although Ni alloys exhibit excellent functional properties such as shape-memory effect and catalytic properties.

In this work, we developed new LMD technology that adding an amount of B(Ni) to the liquid bath such that only a fraction of B(Ni) dissolves from the A-B precursor (Fig.1(b)). The dealloying naturally stops when an equilibrium is reached between solid ligament and liquid phases. In such a system, by immersing a precursor of $A_{1-x'}B_{x'}$ ($x'>x$) in a B_yC_{1-y} bath, the content of B in the precursor decreases until the composition of the solid ligaments reaches $A_{1-x}B_x$ to achieve thermodynamic equilibrium. This is referred to as partial liquid metal dealloying (PLMD) [2].

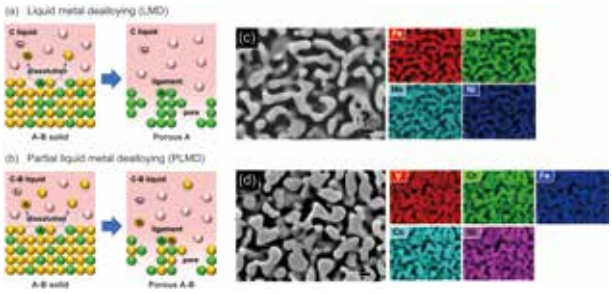

Fig. 1 Schematic illustration showing porous metal formation by (a) LMD and (b) PLMD. SEM image and EDX maps for the Ni-containing nanoporous (c) stainless steel and (d) high-entropy alloy synthesized by PLMD

Using the concept of PLMD, we demonstrated to fabricate austenitic stainless steel (equivalent to SUS316L) and high-entropy alloys. Figure 1(c) shows cross-sections of the microstructures obtained after immersing a $(Fe_{0.657}Cr_{0.194}Ni_{0.134}Mo_{0.015})_{30}Ni_{70}$ precursor in $(Mg_{0.75}Bi_{0.25})_{92}Ni_7Cr_1$ bath at 1023 K for 10 min, followed by etching in nitric acid The EDX maps indicate the uniform distribution of Fe, Cr, Ni, and Mo in the ligaments. The average composition of the porous metal was $Fe_{64.9}Cr_{20.1}Ni_{13.6}Mo_{1.4}$(at.%), showing excellent agreement with the composition range of SUS316L. Figure 1(d) shows $(V_{0.15}Cr_{0.15}Fe_{0.20}Co_{0.25}Ni_{0.25})_{50}Ni_{50}$ precursor immersed in $(Mg_{0.5}Bi_{0.5})_{98.2}Ni_{1.5}Cr_{0.3}$ bath at 1023 K for 30 min. The EDX composition maps acquired from the cross-section of ligaments reveal uniform distribution of the desired elements. Average composition was $V_{14.9}Cr_{11.9}Fe_{18.8}Co_{21.3}Ni_{33.2}$, falling into the definition of high entropy alloy. These ligaments had a face-centered cubic structure in the both porous metals confirmed by the X-ray diffraction spectrum.

References

[1] T. Wada, K. Yubuta, A. Inoue, and H. Kato, Mater. Lett. **65**, 1076 (2011).

[2] T. Wada, P.-A. Geslin, D. Wei, and H. Kato, Commun. Mater. **4**, 43 (2023).

Takeshi Wada and Hidemi Kato (Non-Equilibrium Materials Research Laboratory)
E-mail: takeshi.wada.d7@tohoku.ac.jp, hidemi.kato.b7@tohoku.ac.jp
URL: http://www.nem2.imr.tohoku.ac.jp/index-e.html

Atomic and Electronic Structure in MgO-SiO_2

Understanding disordered structure is difficult due to insufficient information in experimental data. To investigate oxygen packing and network topology in glassy (*g*-) and liquid (*l*-) MgO-SiO_2 based on a comparison with the crystalline topology, we used a combination of diffraction and simulation. We find that the glass-forming ability (GFA) of MgO-SiO_2 binary is dominated by the atomic structure in terms of network topology.

The MgO–SiO_2 system is very important in both glass science and geoscience [1] since *g*-MgO–SiO_2 is a typical binary silicate glass system and crystalline (*c*)-$MgSiO_3$ (enstatite) and *c*-Mg_2SiO_4 (forsterite) are Mg-end members of main components of the Earth's mantle. Liquid Mg_2SiO_4 can be classified as a fragile liquid, while *l*-$MgSiO_3$ is a stronger liquid according to Angell [2]. Particularly, viscosity under high pressure and high temperature is an important thermophysical property to understand magma ocean solidification [3].

In this study, we performed high-energy X-ray diffraction and neutron diffraction measurements on *l*-$MgSiO_3$ and *l*-Mg_2SiO_4 to obtain detailed structural information about the liquids. To investigate atomic configurations with detailed electronic structures of *g*- and *l*-MgO–SiO_2, we conducted advanced density functional – molecular dynamics simulations for *g*- and *l*-MgO–SiO_2 using the measured density of *l*-Mg_2SiO_4 by an electrostatic levitation furnace under microgravity at the International Space Station. Moreover, we performed several topological analyses (ring, polyhedral connection analysis, and persistent homology) on *c*-, *g*-, and *l*-MgO–SiO_2 to extract topological similarity among the crystal, glass, and liquid to understand the relationship between the topology and GFA.

Diffraction measurements and density functional – molecular dynamics simulations demonstrated that the packing of oxygen atoms is an important structural descriptor to understand the difference between $MgSiO_3$ and Mg_2SiO_4 and between glass and liquid [4]. The analysis of electronic and topological structures suggests that an electronic state does not change quite a lot between $MgSiO_3$ and Mg_2SiO_4, and the topological similarity between *c*- and *g*- (*l*-) Mg_2SiO_4 is the signature of low GFA. On the other hand, high GFA *g*- (*l*-) $MgSiO_3$ shows a unique glass topology, which is different from *c*-$MgSiO_3$. These results show that the atomic structure in terms of network topology is an important factor to understand GFA. Systematic comparison among crystal, glass, and liquid is important to understand the nature of glass and liquid.

References

[1] B. Mysen and P. Richet, *Silicate Glasses and Melts*, *Second Edition* (Elsevier, 2019).

[2] C. A. Angell, Science **267**, 1924 (1995).

[3] L. Xie, A. Yoneda, D. Yamazaki, G. Manthilake, Y. Higo, Y. Tange, N. Guignot, A. King, M. Scheel, and D. Andrault, Nat. Commun. **11**, 548 (2020).

[4] Y. Shuseki *et al.*, J. Phys. Chem. A **128**, 716 (2024).

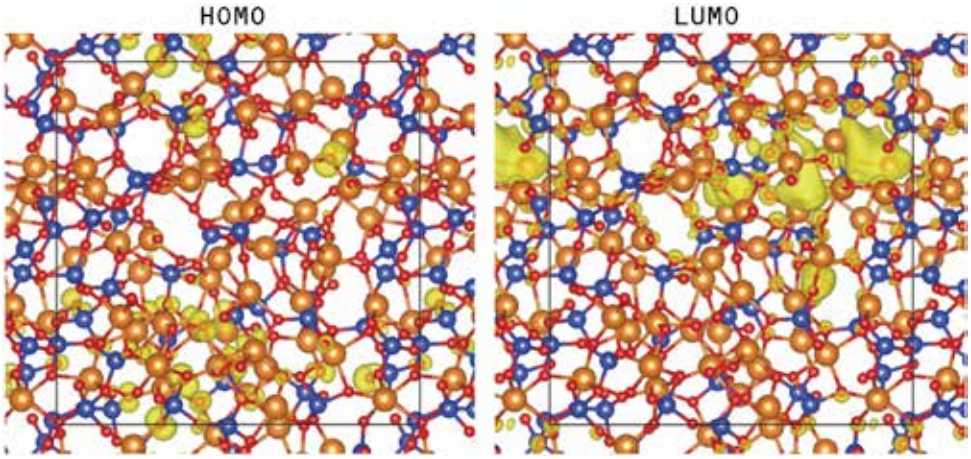

Fig. 1 Isosurface plots of the partial charge density around the HOMO and the LUMO levels for g-$MgSiO_3$.

Junpei Okada (Crystal Chemistry Research Laboratory)
E-mail: junpei.okada.b6@tohoku.ac.jp
URL: http://www.imr.uda-lab.imr.tohoku.ac.jp/index-e.html

International Co-Authored Paper

Calcium Metal Batteries with Long Cycle Life with a Hydride-Based Electrolyte and Copper Sulfide Electrode

A long-cycle-life calcium metal battery is developed using a copper sulfide/carbon (CuS/C) composite and a tailored monocarborane electrolyte of $Ca(CB_{11}H_{12})_2$ in DME/THF, which enables reversible calcium plating/stripping at room temperature. The combination affords a calcium metal battery with a long cycle life of over 500 cycles and capacity retention of 90% based on the capacity of the 10th cycle.

Batteries with Ca metal anodes appear competitive in terms of realizing high energy densities, given the high volumetric/gravimetric capacities (2072 mAh cm^{-3}/1337 mAh g^{-1}) and low reduction potential (–2.87 V vs. the standard hydrogen electrode) of the Ca metal. Additionally, as the charge density of Ca^{2+} (0.49 e $Å^{-3}$) is lower than that of other divalent ions such as Mg^{2+} and Zn^{2+} (1.28 and 1.18 e $Å^{-3}$, respectively), the softness of Ca^{2+} ions induces a tendency to form more covalent bonds with host anions, which may accelerate ion transport and diffusion in electrolytes and cathode materials. These advantageous characteristics of Ca—in addition to its abundance in the crust and environmental compatibility—highlight the significance of Ca metal batteries as a promising post-Li ion battery (LiB) candidate. However, the research and development of Ca metal batteries involve various challenges, including the lack of an efficient electrolyte and a practical cathode that promotes the reversible Ca^{2+} storage reaction [1].

To overcome these limitations, the applicability of a CuS cathode in Ca metal batteries and its electrochemical properties are verified herein. Ex-situ spectroscopy and electron microscopy results show that a CuS cathode comprising nanoparticles that are well dispersed in a high-surface-area carbon matrix can serve as an effective cathode for Ca^{2+} storage via the conversion reaction. This optimally functioning cathode is coupled with a tailored, weakly coordinating monocarborane-anion electrolyte, viz. $Ca(CB_{11}H_{12})_2$ in 1,2-dimethoxyethane(DME) /tetrahydrofuran(THF), which enables reversible Ca plating/stripping at room temperature [2]. The combination affords a Ca metal battery with a long cycle life of over 500 cycles and capacity retention of 92% based on the capacity of the 10th cycle. Furthermore, the battery can deliver a reasonable energy density of 144 Wh kg^{-1} at a high power density of 4000 W kg^{-1}, which is comparable to that of previously reported dual-cation-system Ca metal batteries.

The prototype CuS/Ca batteries with the $Ca(CB_{11}H_{12})_2$ in DME/THF electrolyte exhibited higher performance than state-of-the-art Ca and cycle life. This study highlights the potential metal batteries in terms of both the rate capability of developing practical batteries using Ca metal [3]. The use of cathodes at voltages >3 V could enable improvements in the energy density of Ca metal batteries and facilitate the use of Ca-ion batteries as practical alternatives to existing LIBs.

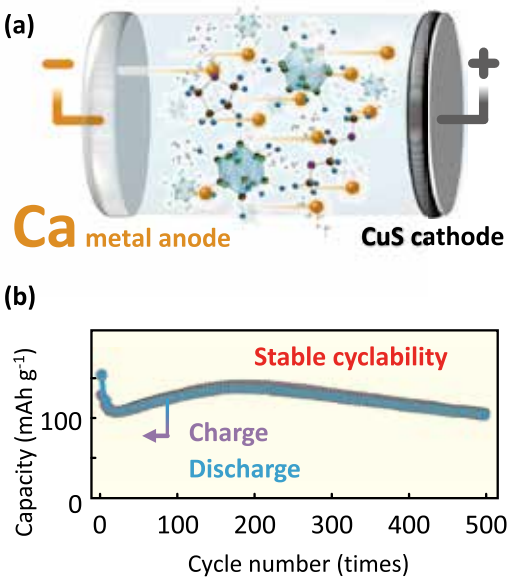

Fig. 1 (a) Schematic of a prototype Ca metal battery. The battery comprises a Ca^{2+} storing positive electrode containing the CuS cathode and Ca metal anode with a hydrogen cluster electrolyte. (b) Cycling performance of the Ca–CuS battery.

References

[1] M. E. Arroyo-de Dompablo, A. Ponrouch, P. Johansson, and M. R. Palacin, Chem. Rev. **120**, 6331 (2020).

[2] K. Kisu, S. Kim, T. Shinohara, K. Zhao, A. Zuttel, and S. Orimo, Sci. Rep. **11**, 7563 (2021).

[3] K. Kisu, R. Mohtadi, and S. Orimo, Adv. Sci. **10**, e2301178 (2023).

Kazuaki Kisu and Shin-ichi Orimo (Hydrogen Functional Materials Research Laboratory)
E-mail: kazuaki.kisu.b2@tohoku.ac.jp
URL: http://www.hydrogen.imr.tohoku.ac.jp/en/index.html

International Co-Authored Paper

Alkali Mono-Pnictides: A New Class of Photovoltaic Materials by Element Mutation

Selenium-based solar cells, with a maximum efficiency of 6.5%, can be improved using element mutation with Group 15 elements (P, As, Sb) and alkali metals (Li, Na, K, Rb, Cs). NaP shows promise due to its abundant elements, suitable band gap, high absorption, and effective charge carrier properties, though P vacancies may limit its performance. Solutions for reducing these vacancies and preliminary NaP sample results with a 1.66 eV band gap indicate potential in photovoltaic technology.

In 1873, Willoughby Smith reported that selenium (Se) exhibits photoconductivity and three years later, Adams and Day demonstrated the first solid-state solar cell using Se. However, the best power conversion efficiency reaches only 6.5% [1]. One contributing factor is the larger band gap of 1.8 eV compared to the optimal value around 1.3–1.5 eV. Substituting elements while maintaining charge neutrality, often referred to as element mutation is a common practice in the search for new materials. Instead of simply substituting one element with two, while keeping the average oxidation state, we introduce ions into the vacant sites within the structure, and mutate the elements while preserving *overall neutral charge*.

Because Se is a Group 16 element in a neutral charge state, we replace Se with -1 anions and intercalate +1 cations, namely alkali metals (*M*), between the chains to maintain a charge balance (see Fig. 1). To retain the chain-like structures in *t*-Se, we consider Group 15 pnictogens as anions (*Pn*).

One advantage of the *MPn* composition is that the physical properties can be optimized by changing the cation-anion combinations. Indeed, the band gap is controllable within a range of optimal band gaps for solar cells as shown later. Another advantage is the cations should attract the anion chains more strongly, which results in greater stability.

In this study, we performed first principles calculations on the phase stability and optoelectronic properties of *MPn* compounds to investigate the potential as photovoltaic materials [2]. It is found that a series of *MPn* cover the appropriate band gap range for solar cells and exhibit relatively strong optical absorption onsets and low electron and hole effective masses. We also calculated the point defects in NaP, a representative of *MPn* composed of non-toxic and earth abundant elements. Our calculations reveal that P vacancies (V_P) have relatively low formation energies and show deep levels, which should be detrimental to photovoltaic efficiency based on the Shockley-Read-Hall (SRH) theory for non-radiative recombination. Indeed, calculations of non-radiative carrier capture rates reveal the carrier recombination by V_P is likely to be significant. To reduce V_P concentrations, we propose to control the Fermi level by adjusting growth conditions and/or introducing dopants. To verify our calculations, we synthesized NaP and measured its direct band gap using a diffuse reflection measurement. Our experiment shows that the observed direct band gap is 1.66 eV, which closely matched the calculated direct band gap of 1.62 eV.

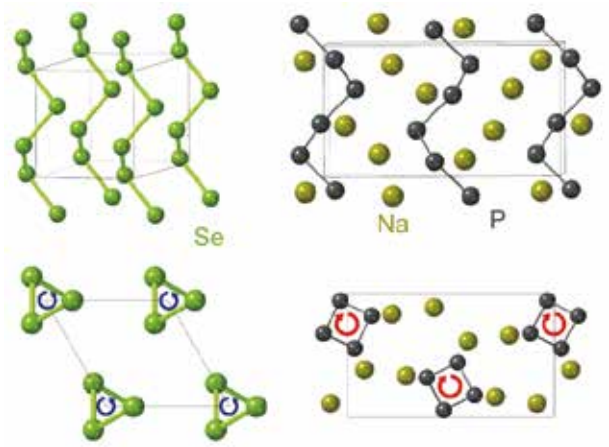

Fig. 1 Crystal structures of (left) trigonal Se and (right) orthorhombic NaP. The blue and red circled arrows depict the helical chain rotation directions from the back of the paper to the front.

References

[1] T. K. Todorov, S. Singh, D. M. Bishop, O. Gunawan, Y.-S. Lee, T. S. Gershon, K. W. Brew, P. D. Antunez, and R. Haight, Nat. Commun. **8**, 682 (2017).

[2] Y. Kumagai, S. R. Kavanagh, I. Suzuki, T. Omata, A. Walsh, D. O. Scanlon, and H. Morito, PRX Energy **2**, 043002 (2023).

Yu Kumagai (Multi-Functional Materials Science Research Laboratory)
E-mail: yukumagai@tohoku.ac.jp
URL: https://kumagailab.imr.tohoku.ac.jp/en/

Stabilizing $LiMn_2O_4$-Based Spinel Cathode Materials for Advanced Photo-Rechargeable Batteries

Photo-rechargeable batteries (PRBs), which integrate solar-energy harvesting and storage, are promising for sustainable energy use. However, limited cathode materials have hindered their development. Here we provide a fundamental understanding of the structure design of $LiMn_2O_4$-based spinel cathode materials and show that $LiMn_{1.5}Fe_{0.5}O_4$ exhibits a remarkably high stability during photocharging.

Utilizing solar energy is key to establishing a sustainable society. Although solar cells can convert solar energy to electricity, they must be connected to rechargeable batteries for storing the energy. To minimize the size and cost, an integrated system called photo-rechargeable batteries (PRBs) has been proposed. Figure 1(a) shows a schematic illustration of a kind of PRB, where electrons are excited under illumination by a photoactive material located with a cathode material [1]. If the energy levels of holes and excited electrons are adequate compared with those of the cathode and anode materials, the battery can be photocharged without external electric charging, which is necessary for usual batteries.

One of the serious problems is the lack of cathode materials suitable for PRBs due to the stability under illumination. In our previous study [1], we demonstrated the photocharging of a 4-V class $LiMn_2O_4$ cathode for the first time by using TiO_2 nanoparticles and $K_2S_2O_8$ as an electron acceptor. Li extraction from $LiMn_2O_4$ proceeds under the illumination of UV-visible light (300–600 nm); however, an obvious irreversible capacity was observed for long-term illumination. Further analyses suggested that it was probably because of the disproportionation of Mn^{3+} on the surface of the particle, resulting in the dissolution of Mn^{2+} into the electrolyte.

Partial replacement of Mn with other elements is an effective way to prevent degradation due to the disproportionation. To investigate it, here we compared the photocharging performance of $LiMn_{1.5}M_{0.5}O_4$ (M = Fe, Co, Ni, Zn) [2], in addition to $LiMn_2O_4$. While divalent Ni^{2+} and Zn^{2+} highly stabilized the structure, the capacity from Mn^{3+} decreased because of the charge compensation. In the case of Co, its high catalytic activity under illumination would lead to side reactions. On the contrary, trivalent Fe^{3+} was appropriate both in terms of stability and capacity, as shown in Fig. 1(b) and 1(c). Specifically, the reversible charging rate was kept at approximately 23 mA/g even for the 2-h photocharging process.

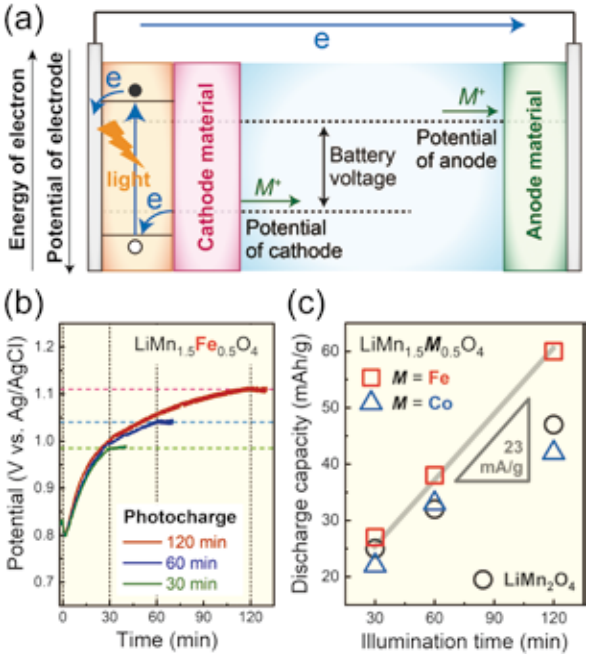

Fig. 1(a) Charging mechanism of PRBs [1]. (b) Potential change of $LiMn_{1.5}Fe_{0.5}O_4$ during the photocharging process. (c) Discharge capacity of $LiMn_{1.5}M_{0.5}O_4$ (M = Fe, Co) and $LiMn_2O_4$ after the photocharging process [2].

Towards the development of practical PRBs, there are remaining issues such as the structure design of anode and electrolyte. Although the current system is a half-cell only focusing on the cathode performance, we believe that this work provides fundamental design guidelines for the electrode materials of PRBs. In addition, spinel oxide is highly designable, and therefore further improvements in the photocharging performance would be achieved in the future.

References

[1] K. Shimokawa, S. Matsubara, A. Okamoto, and T. Ichitsubo, Chem. Commun. **58**, 9634 (2022).

[2] K. Shimokawa, S. Matsubara, T. Kawaguchi, A. Okamoto, and T. Ichitsubo, Chem. Commun. **59**, 7947 (2023).

Kohei Shimokawa (Exploratory Research Laboratory)
E-mail: kohei.shimokawa.b7@tohoku.ac.jp
URL: http://www.imr.tohoku.ac.jp/en/about/divisions-and-centers/research-division/33.html

Electronic Materials

IMR KINKEN Research Highlights 2024

GIMRT

Automated Pulsed Magnet System for Neutron Diffraction Experiments

An automatic operational pulsed magnet system has been developed for high magnetic field neutron diffraction at the Materials and Life Science Experimental Facility in Japan Proton Accelerator Research Complex(J-PARC) by the collaboration research between IMR and J-PARC. The combinations of 4 K and 35 T is available with a wide scattering angle of 42 degrees.

Neutron diffraction is a unique method to determine the magnetic structure in magnetic ordered state. When strong magnetic fields are applied to magnetic materials, varieties of magnetic field induced phase transitions such as metamagnetic transition, spin reorientation, spin density wave etc. are observed. To determine the change of magnetic structure in such phase transitions, it is necessary to conduct a neutron diffraction in high magnetic fields.

Application of pulsed magnetic field enables the high magnetic field neutron diffraction in the magnetic field beyond 30 T. Pulsed magnetic field experiments has been conducted in JRR3, J-PARC, SNS, ILL and ISIS with the leading contribution of the magnetism division of IMR. In J-PARC, combinations of white neutron and a pulsed magnetic field enables us to access a wide range of reciprocal space, yet accumulation of a few hundred shots is required to obtain a practical statistic. One of the most important points is how to implement a pulsed magnet system into the user operation spectrometer. The key issue is the long-time automatic operation capability with the less contribution of a specialist.

We have developed an automatic operational pulsed magnetic system up to 35 T to achieve this important objective. We have installed a GM-refrigerator for sample cooling. It has two merits. One is the easy operation for low temperature as user do not need experience of handling liquid He. The other is the simpler vacuum chamber setup with a wide scattering angle. The scattering angle is increased from 28 degree to 42 degree. In the wider angle, most of magnetic scattering in low-$\boldsymbol{q}$ region can be covered easily.

Another key improvement is the increase of the magnetic field from 30 T to 35 T by using a new compact and reinforced coil. The coil is cooled down by the liquid nitrogen and thus the cooling efficiency is high compared with the solid contact cooling. The liquid nitrogen is automatically filled during the experiment and the long-term automatic running is possible without the access to the cryostat. It is also important from the viewpoint of safety, because user is not required to access the pulsed coil during experiments.

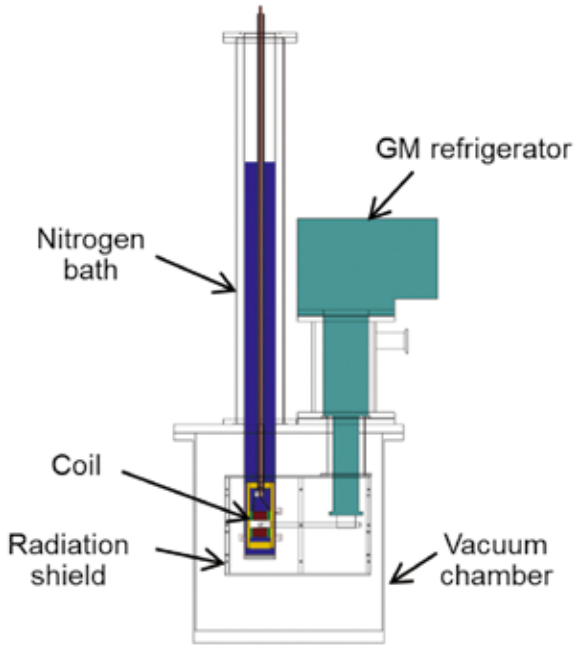

Fig. 1(a) Schematic view of the automatic 35 T pulsed magnet system for neutron diffraction [1].

For the automatic operation, the sensing of the system anomaly such as a irregular discharge or coil break down is important. The present system has a controller to examine the output waveform of a pulsed magnetic system during the operation. If a deviation from the standard magnetic field curve is observed, the system dumps into the locked mode and the pulsed field generation is halted automatically.

In summary, our new automatic pulsed magnet system for neutron diffraction provides user the access for the extreme environment combining 35 T and 4 K at J-PARC.

References

[1] M. Watanabe, T. Kihara, and H. Nojiri, Quantum Beam Science **7(1)**, 1 (2023).

Hiroyuki Nojiri (Magnetism Research Laboratory)
E-mail: hiroyuki.nojiri.e8@tohoku.ac.jp
URL: http://www.hfpm.imr.tohoku.ac.jp

Topochemical Reduction Leads to Superconducting Infinite-Layer Nickelate Thin Films

The recent discovery of superconductivity in infinite-layer nickelates has garnered significant interest due to their potential analogy to high Curie temperature T_c cuprates. Through topochemical reduction, the infinite-layer structure has been synthesized from the perovskite structure. By tuning the reduction temperature precisely, we achieved highly crystalline films exhibiting a higher T_c. Our results emphasize the critical role of the topochemical reduction process for stabilization of high-T_c phase of the superconducting infinite-layer nickelate thin films.

The discovery of nickelate superconductors creates exciting opportunities for exploring unconventional superconductivity, due to their potential analogy to high Curie temperature T_c cuprates, where both cases derive from doping a transition metal $3d^9$ configuration [1]. Superconductivity has been observed in nanoscale thin films, which are epitaxially stabilized through a topochemical reduction from the perovskite precursor phase. This reduction process selectively removes apical oxygen atoms from Ni-O octahedra, resulting in low-valence layered nickelates where the oxidation state of Ni ions changes from Ni^{3+} ($3d^7$) to Ni^{+} ($3d^9$) (Fig. 1a). Although some notable distinctions, such as the multi-band nature of the electronic structure associated with the rare-earth $5d$ orbitals and the absence of magnetic long-range order in nickelates, have been discussed, experimental efforts have been limited due to the challenges of material synthesis. In this context, understanding and achieving significant advances in the synthesis process are crucial.

With this notion, we address this critical issue by systematically tuning the reduction temperature [2]. The precursor phase of $La_{1-x}Sr_xNiO_3$ was grown by pulsed laser deposition, and the infinite-layer phase was achieved by ex-situ low-temperature annealing within sealed glass tubes containing CaH_2 powder. Gradual tuning of the topochemical reduction temperature from 280 to 410°C leads to the transformation of nickelate films from an insulating state into a superconducting state (Fig. 1b). Notably, the superconducting transition temperature T_c reaches ~14 K for Sr content $x = 0.20$, which is higher than that reported in previous studies with same composition films. Furthermore, systematic optimization results in an expansion of the superconducting dome in the temperature versus Sr content x phase space, with a higher T_c and a wider Sr content x regime.

Our findings provide insight into the topochemical reduction process and its role in the electronic transport properties, with significant implications for the synthesis of nickelate superconductors. The optimized process will contribute to the stabilization of highly crystalline infinite-layer nickelate films, which leads to the further studies for revealing similarities and differences in superconductivity in nickelates and cuprates.

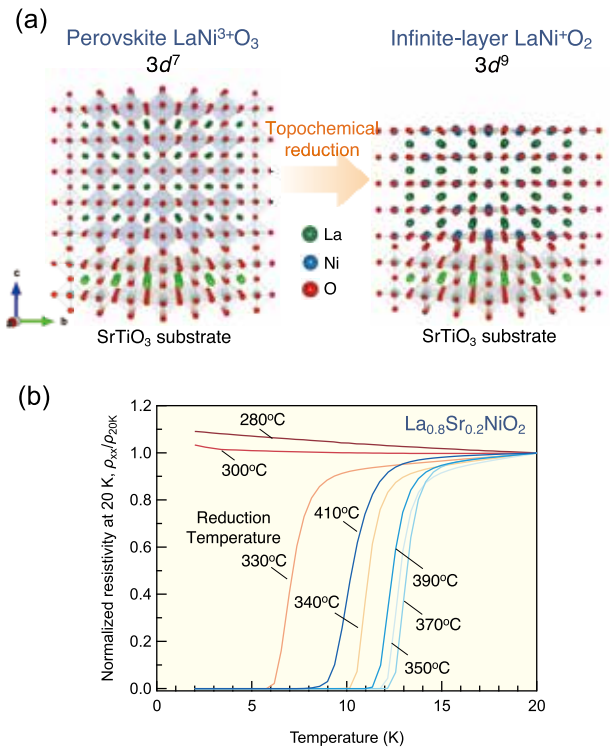

Fig. 1(a) Simplified picture of topochemical transformation of perovskite $LaNiO_3$ films into infinite-layer $LaNiO_2$ films. (b) Temperature dependent resistivity ρ_{xx}/ρ_{20K}-T curves for $La_{0.8}Sr_{0.2}NiO_2$ films upon topochemical reduction. Resistivity is normalized at 20 K.

References

[1] D. Li, K. Lee, B. Y. Wang, M. Osada, S. Crossley, H. R. Lee, Y. Cui, Y. Hikita, and H. Y. Hwang, Nature **572**, 624 (2019).

[2] M. Osada, K. Fujiwara, T. Nojima, and A. Tsukazaki, Phys. Rev. Mater. **7**, L051801 (2023).

Motoki Osada (Low Temperature Physics Research Laboratory)
E-mail: mosada@tohoku.ac.jp
URL: http://mu.imr.tohoku.ac.jp/?page_id=1128&lang=en

Preformed Cooper Pair Near Mott Transition Probed by NMR

A peculiar electronic state, referred to as the pseudogap-like state, emerges near the correlation-driven Mott transition. In this study, we demonstrate that unconventional preformation of Cooper pairs is the origin of the pseudogap-like behavior near the Mott transition in layered organic superconductors. Our findings clarify that Cooper pair preformation is significantly enhanced on the verge of the Mott transition.

A layered organic material, κ-$(ET)_2X$, where ET represents bis(ethylenedithio)-tetrathiafulvalene, with a half-filled band exhibits unconventional superconductivity (d-wave) emerged from Mott insulators without doping but by varying the bandwidth, which controls the relative strength of the interactions to the kinetic energy. It is well recognized that the application of physical pressure and/or chemical pressure by anion X substitution finely tunes the interaction strength. In particular, κ-$(ET)_2Cu[N(CN)_2]Br$ with all protons in ET substituted by deuterons (abbreviated to κ-dBr) is on the verge of the correlation-driven Mott transition(Fig. 1(a)). In ordinary metals, nuclear spin-lattice relaxation rate divided by temperature, $(T_1T)^{-1}$, is independent of temperature and magnetic field because the dynamic spin susceptibility of conduction electrons does not sensitively vary with those parameters. However, the metallic phase of κ-dBr shows an anomalous decrease in $(T_1T)^{-1}$ on cooling from above T_c, which is compared to the pseudogap in the high-T_c cuprates.

The present work [1] explores the anomalous suppression of spin excitations in κ-dBr through ^{13}C NMR under tuning interaction strength by He-gas pressure and systematically suppressing superconductivity by magnetic fields over a 20-fold range (0.9 to 18 T). We found that the anomalous decrease in spin excitations on cooling occurs mainly in the channel of antiferromagnetic fluctuations very probably with $\mathbf{Q} = (\pi, \pi)$, which is enhanced near the Mott transition(Fig. 1(b)), and the anomaly fades out along with superconductivity under increasing magnetic field(Fig. 1(c)). Our further investigation of different materials, which are located in different "distances" from the Mott transition by chemical pressure, suggests that the phenomena cannot be explained by conventional superconducting amplitude fluctuations but is an indication of unconventional superconducting phase fluctuations due to preformation of Cooper pairs.

We note that this observation is free from the intricate issue of competing or coexisting orders as observed in high-T_c cuprates, because in the measured temperatures, pressures, and magnetic fields, the NMR spectra do not show any splitting, broadening or complicated structures indicative of symmetry breaking such as charge order in a metallic phase.

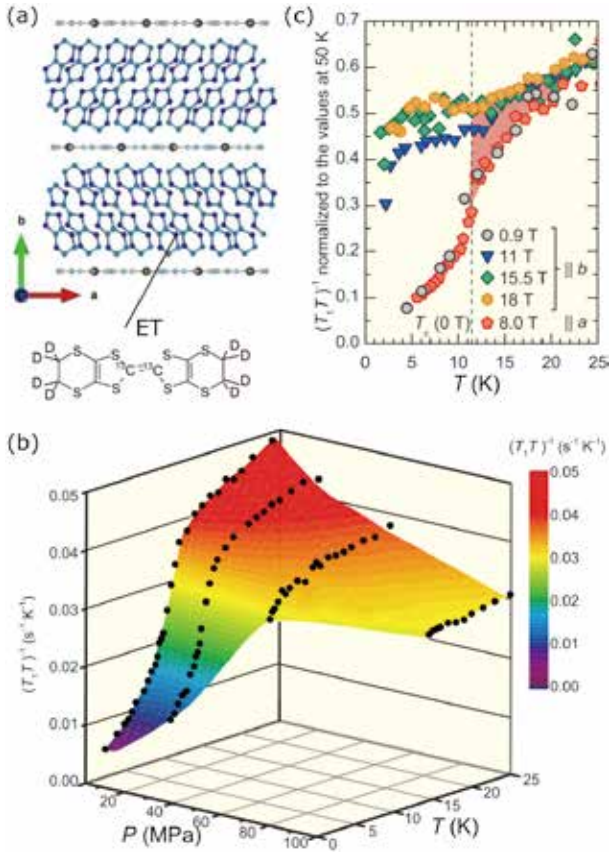

Fig. 1(a) Crystal structure of κ-dBr. (b,c) pressure (b) and magnetic field (c) dependence of anomalous behavior of $(T_1T)^{-1}$.

References

[1] T. Furukawa, K. Miyagawa, M. Matsumoto, T. Sasaki, and K. Kanoda, Phys. Rev. Research **5**, 023165 (2023).

Tetsuya Furukawa (Low Temperature Condensed State Physics Research Laboratory)
E-mail: tetsuya.furukawa.c1@tohoku.ac.jp
URL: http://cond-phys.imr.tohoku.ac.jp/index_e.html

Topological Surface Acoustic Wave

While the topological aspect of the electronic state has been attracting much attention recently, the concept of topology can be applied also to the phononic state. Here we demonstrate the formation of a topological phononic edge state between two mutually inverted topological phononic crystals fabricated on a surface acoustic wave device.

To realize the topological edge state of acoustic waves, we fabricate periodically arranged nanopillars forming honeycomb lattices on a surface acoustic device [1]. Their unit cell consists of two different Au cylinder-like pillars. They are expected to work as phononic crystals that show the acoustic version of the quantum valley Hall effect. To realize a topological waveguide, we fabricate two honeycomb lattices next to each other, which have valley Chern numbers of opposite signs. They are denoted as A and B lattices as shown in Fig. 1. The upper panel of Figure 2 shows the atomic force microscopy AFM image of the fabricated A and B lattices.

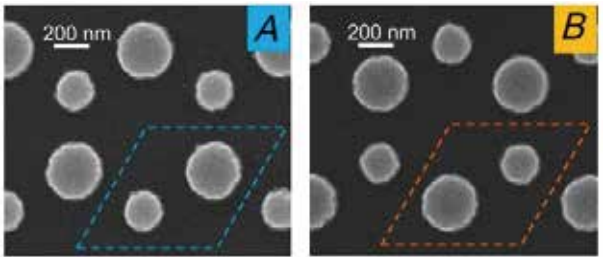

Fig. 1 Scanning electron microscopy SEM images of two topological phononic crystals.

Then, we observe the image of topological edge state, utilizing the technique of pulse-type microwave impedance microscopy MIM, which can visualize the surface acoustic wave on the phononic crystal. For this purpose, we develop a pulse-type MIM imaging system based on a commercial AFM system. The unique feature that differentiates this from conventional MIM systems is the use of pulse-modulated microwaves with a pulse duration of 150 ns. In this system, one can separate SAW and electromagnetic crosstalk in the time domain. The lower panel of Figure 2 shows the MIM image of a surface acoustic wave with a frequency of 2.35GHz propagating on the A and B lattices. At this frequency, the bulk surface acoustic state is gapped but the edge state should emerge according to a band calculation. This is in agreement with the experimental observation; the SAW intensity is discernible only around the interface.

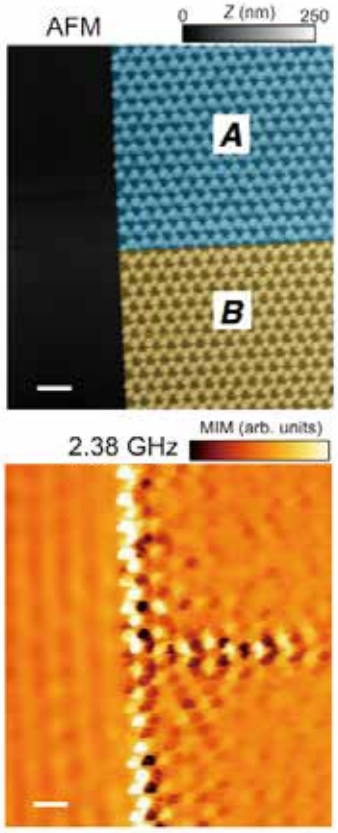

Fig. 2 Upper panel: AFM image of A-B domain boundary. Lower panel: MIM image of A-B domain boundary at 2.38 GHz. Scale bars are 2 μm.

Thus, we have succeeded in demonstrating topological SAW mode around 2.4 GHz in a honeycomb lattice made of metallic pillars on a $LiNbO_3$ piezoelectric substrate. While a similar topological edge state was previously realized in a purely two-dimensional system, the present result shows that the topological edge mode traveling along the surface is robust against hybridization with the interior Bulk modes of the substrate. The method of topological patterning on a substrate seems quite useful for implementing topological waveguides and other functionalities into practical acoustic devices working at gigahertz frequencies. The achievements may contribute to the further development of SAW devices for various purposes.

References

[1] Y. Nii and Y. Onose, Phys. Rev. Appl. **19**, 014001 (2023).

Yoshinori Onose (Quantum Functional Materials Physics Research Laboratory)
E-mail: yoshinori.onose.b4@tohoku.ac.jp
URL: http://www.imr.tohoku.ac.jp/en/about/divisions-and-centers/research-division/08.html

New Hexagonal Approximant ζ´-AlMnCo

The structure of ζ´-$Al_{80}Mn_{16}Co_4$ was analyzed using single-crystal X-ray diffraction. The diffraction pattern indicated that the ζ´-AlMnCo phase has a hexagonal unit cell with a space group $P6_3/m$, a = 30.5173(5) Å, c = 12.4742(2) Å, and the a-axis is √3-times as large as that of the ζ-phases in the Al-Cr-Cu and Al-Cr-Ni systems. Mn atoms prefer icosahedral coordination similar to that of Cr in the ζ-phase, and the Co atoms are located in the interstitial area formed by the connection of the icosahedra [1].

ζ´-$Al_{80}Mn_{16}Co_4$ sample was prepared from an ingot of $Al_{80}Mn_{17}Co_3$. The solidified ingot was crushed into grains several millimeters in size, heated in an evacuated furnace at 1000 °C for 24 h, and subsequently cooled to 750 °C. A single-crystal sample with dimensions of 0.079 × 0.071 × 0.054 (mm) was cut from the prepared sample. Intensity measurements were performed on the sample using a Rigaku XtaLAB Synergy-S diffractometer equipped with a HyPix–6000HE hybrid photon counting (HPC) detector and a Mo microfocus-sealed X-ray source. Least-squares refinement was performed using the SHELXL software program.

Figures 1(a) and (b) indicate that the structure of ζ´-$Al_{80}Mn_{16}Co_4$ is composed of rod structures: hR, hR´, and tR. The overall geometrical features of hR and hR´ appear to be similar but differ based on the presence or absence of Co at the center. Atomic arrangements in the central area and harmonic displacements of the Al sites in the rod structure also indicate the contrast of the Co distributions. These structural features suggest that the distribution of Co and the corresponding structural realization is an important factor in the development of superstructures.

The structures of decagonal and icosahedral quasicrystals in Al–Mn-based systems are composed of pentagonal columnar clusters in Al_3Mn, an icosahedral Mackay cluster in α-AlMnSi, and a Bergman cluster. Similar atomic arrangements can be found in ζ´-AlMnCo structure and Figure 2 shows some selected examples. The I3 cluster has three local five-fold rotational axes along the directions of the vertex-shared icosahedral pair and the pentagonal columnar cluster of an icosahedron around Mn (Mn–$Al_{10}Mn_2$), a bicapped pentagonal prism around Al (Al–Mn_2Al_{10}), and an icosahedron around Mn (Mn–$Al_{10}Mn_2$) as shown in Fig. 2(a). This columnar cluster could be further extended by I-type connections along the a-axis. Figure 2(b) shows an icosahedral cluster around Mn13. The first neighbor shell around the Mn13 site is an icosahedral 12 Al, and the second shell shows an icosahedral

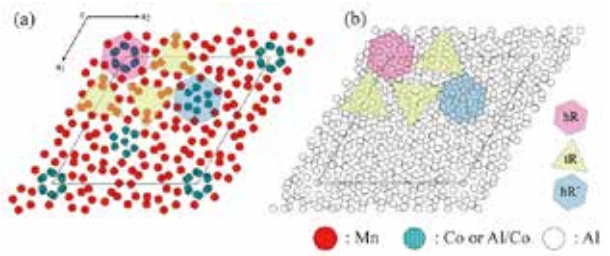

Fig. 1 The c-axis projection of ζ´-AlMnCo and ζ-AlCrNi structures. (a) heavy metal sites, (b) Al sites of ζ´-AlMnCo.

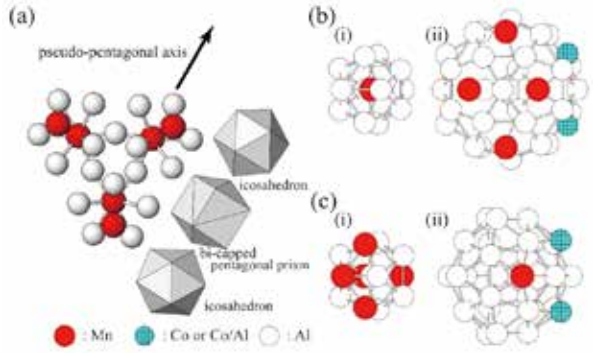

Fig. 2 The pentagonal columnar and icosahedral clusters in ζ´-AlMnCo.

symmetry with a harmony of icosidodecahedron and truncated icosahedron. Interestingly, another partial Bergman cluster is observed around the icosahedrally coordinated Al. Figure 2(c) shows a partial Bergman cluster around Al21. The Al21 site is surrounded by seven Al and five Mn atoms; the second shell is a dodecahedron, and the seven pentagons are capped by Al, Co, or Mn in the Bergman fashion.

References

[1] Y. Makino, T. Kawamata, and K. Sugiyama, J. Phys.: Conf. Ser. **2461**, 012010 (2023).

Kazumasa Sugiyama (Chemical Physics of Non-Crystalline Materials Research Laboratory)
E-mail: kazumasa.sugiyama.e6@tohoku.ac.jp
URL: https://www.imr.tohoku.ac.jp/en/about/divisions-and-centers/research-division/15.html

GIMRT International Co-Authored Paper

CO_2-Switched Porous Magnet with Long-Range Order

This study presents the first CO_2-responsive magnet creation by modifying a paramagnetic compound with CO_2, leading to an antiferromagnetic state. This transformation, driven by electron transfer during CO_2 adsorption/desorption, also alters electrical conductivity, offering potential for multifunctional molecular devices.

In the era of the Internet of Things (IoT), there is a growing need for smart sensors that drive the development of multifunctional materials. Among them, magnetic porous coordination polymers (PCPs) and metal-organic frameworks (MOFs) can change their physical properties in response to environmental stimuli, such as electric and magnetic fields, light, temperature, or gaseous adsorbates. Such gas-responsive materials are particularly promising because of their rapid and reversible nature. However, the investigation of gas-responsive porous magnets applicable to ubiquitous gases such as O_2, N_2, CO_2, and so on (hereafter referred to as common gases) is still in its infancy.

Some reasons likely arise from: i) the conflict between the magnetic ordering and porosity in a single material because shorter organic linkers are generally associated with stronger magnetic coupling but consequently produce smaller pores; ii) the necessity of thorny intrinsic spin modifications from structural malformations induced by gas adsorbates; and iii) the difficulty in changing the coordination environment considerably via gas adsorption, as observed in magnetic sponges. This is probably due to the relatively weak interactions between the common gases and porous magnet frameworks. Due to these challenges, there have been few relevant reports on gas-responsive magnets. Recently, studies have progressed in layered electronic–state–flexible magnets, for which only three examples have been reported: (i) a paramagnetic O_2-sensitive magnet, in which the magnetic interaction between ferrimagnetically ordered layers was changed from ferromagnetic to antiferromagnetic coupling via magnetic exchange coupling with introduced paramagnetic O_2; (ii) a CO_2-responsive magnetic phase change, where the interlayer-accommodated CO_2 molecules induced an increment of interlayer distance directly associated with the sign of interlayer magnetic interaction; and (iii) a CO_2-responsive magnetic erasure, where a ferrimagnet was converted into a paramagnet by CO_2 adsorption via electronic state modulation. However, in contrast to the magnetic phase transition that involves magnet erasure, magnet creation, that is, the formation of spontaneous magnetization through gas adsorption, has not yet been reported.

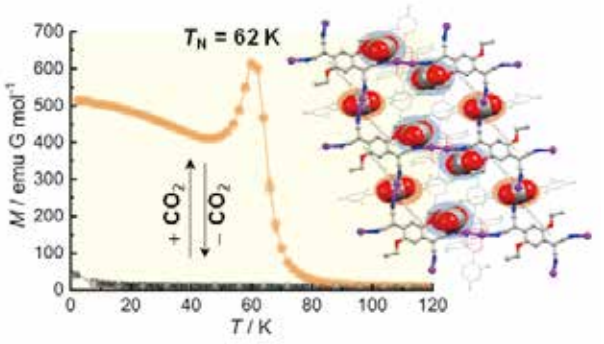

Fig. 1 Field-cooling magnetization curves at H = 100 Oe between **1** (black) and **1**⊃**CO₂** (orange) upon dosing of CO_2 and evacuation. Inset shows the crystal structure of **1**⊃**CO₂**.

We report a CO_2-induced antiferromagnet with a Neel temperature of 62 K modified from a paramagnetic charge-flexible layered compound, [{Ru_2(2,4-F_2ArCO_2)$_4$}$_2$TCNQ(OEt)$_2$] (**1**; 2,4-F_2ArCO_2^- = 2,4-difluorobenzoate; TCNQ(OEt)$_2$ = 2,5-diethoxy-7,7,8,8-tetracyanoquinodimethane), in which three molar equivalents of CO_2 were accommodated at a CO_2 pressure of 100 kPa (Fig. 1) [1]. The magnetic change originates from charge fluctuation due to the transfer of electrons moving from the electron donor to the electron acceptor unit or vice versa, resulting in a change in the electron distribution induced by CO_2 adsorption/desorption in the donor-acceptor-type charge transfer framework. Owing to the reversible electronic state change upon CO_2 adsorption/desorption, these magnetic phases are switched, accompanied by modification of the electrical conductivity, which is boosted by CO_2 accommodation. This is the first example of the creation of a CO_2-responsive magnet that is promising for novel molecular multifunctional devices.

References

[1] J. Zhang, W. Kosaka, Q. Liu, N. Amamizu, Y. Kitagawa, and H. Miyasaka, J. Am. Chem. Soc. **145**, 26179 (2023).

Hitoshi Miyasaka (Solid-State Metal-Complex Chemistry Research Laboratory)
E-mail: junzhang@whu.edu.cn, hitoshi.miyasaka.e7@tohoku.ac.jp
URL: http://www.miyasaka-lab.imr.tohoku.ac.jp/cn5/HOME-Eng.html

Impact of Epitaxial Growth on Spin Current Transmission in Antiferromagnetic Insulator NiO

We investigated the spin current transmission in epitaxial and polycrystalline NiO antiferromagnetic insulators. Exploiting the thermo-spin effect measurement technique, we found that the epitaxial NiO exhibits non-monotonic spin current transmission with respect to NiO layer thickness, while this behavior becomes smeared out in the polycrystalline NiO. This difference is partly attributed to the difference in the NiO layer thickness dependence of antiferromagnetic order between epitaxial and polycrystalline NiO, suggesting that the improvement of antiferromagnetic order is pronounced with epitaxial growth.

Antiferromagnets possess great potential in the field of spintronics as an alternative to ferromagnets owing to their unique characteristics: robustness to external magnetic field, low magnetic stray field, and terahertz resonance. Since antiferromagnets can achieve effective spin injection, propagation, and conversion, their spin transport properties have been intensively studied. NiO is one of the representative antiferromagnetic insulators, and its spin current transmission has been investigated. While the majority of spin and/or magnon transport studies have focused on polycrystalline NiO, the exploration of epitaxial NiO remains limited. Furthermore, reported values for the spin transmission length in epitaxial NiO films vary widely: ranging from ~2 nm [1] to well over 100 nm [2]. Thus, more systematic investigation is indispensable to unravel the physics behind.

This study focuses on the effect of epitaxial growth on spin current transmission in NiO films. As illustrated in Fig. 1(a), the thermo-spin effects that output a heat current in Pt/NiO/$Co_{20}Fe_{60}B_{20}$ (CoFeB) trilayer are used as a probe of the spin current transmission in NiO. The Pt(10 nm)/NiO(t_{NiO})/CoFeB(20 nm) films were deposited on MgO(111) substrates using magnetron sputtering. By controlling the sputtering condition, epitaxial and polycrystalline NiO films were grown. To evaluate the spin current transmission in NiO, we investigated t_{NiO} dependence of the normalized temperature amplitude induced by thermo-spin effects A_{odd}/E, which was detected through the use of lock-in thermoreflectance method [3]. We found that the t_{NiO} dependence of A_{odd}/E for epitaxial NiO exhibits nonmonotonic behavior, which becomes less remarkable in polycrystalline NiO [Fig. 1(b)]. This is clearly different from the previous studies reporting that the dependence of spin current transmission on t_{NiO} exhibited a simple exponential decay [1]. The inset of Figure 1(b) shows the coercivity H_c of CoFeB layer in Pt(10 nm)/NiO(t_{NiO})/CoFeB(3 nm) stacks as a function of t_{NiO}. H_c drastically increases with increasing t_{NiO} from 5 to 10 nm for epitaxial NiO,

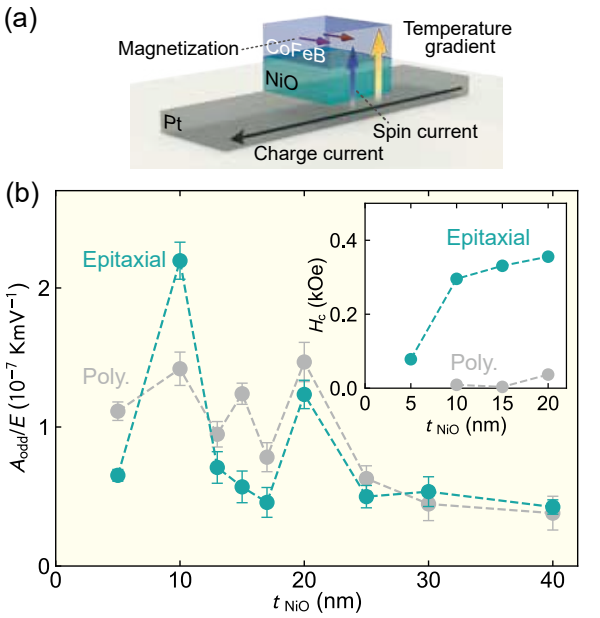

Fig. 1(a) Schematic of spin current transmission measurement through the thermo-spin effects. (b) t_{NiO} dependence of A_{odd}/E. Inset shows H_c as a function of t_{NiO}.

suggesting that the antiferromagnetic order is strengthened and the drastic change of A_{odd}/E at t_{NiO} = 10 nm for epitaxial NiO is attributed to the improved antiferromagnetic order. These results suggest that the spin current transmission in epitaxial NiO cannot be explained solely within the framework of simple magnon diffusion. Although further investigation is required to understand the t_{NiO} dependence behavior fully, this study has provided essential insights into the spin current transmission in the epitaxial NiO film.

References

[1] L. Baldrati, C. Schneider, T. Niizeki, R. Ramos, J. Cramer, A. Ross, E. Saitoh, and M. Kläui, Phys. Rev. B **98**, 014409 (2018).
[2] T. Ikebuchi, Y. Kobayashi, I. Sugiura, Y. Shiota, T. Ono, and T. Moriyama, Appl. Phys. Express **14**, 123001 (2021).
[3] T. Yamazaki, T. Seki, T. Kubota, and K. Takanashi, Appl. Phys. Express **16**, 083003 (2023).

Takumi Yamazaki and Takeshi Seki (Magnetic Materials Research Laboratory)
E-mail: takumi.yamazaki.d5@tohoku.ac.jp
URL: http://magmatelab.imr.tohoku.ac.jp/

International Co-Authored Paper

Quasi-Two-Dimensional Fermi Surfaces Detected by Quantum Oscillations in Spin-Triplet Superconductor UTe_2

Using our ultra-clean single crystal of UTe_2, we successfully observed the quantum oscillations of magnetization, that is de Haas-van Alphen effect, and clarified two quasi-two-dimensional Fermi surfaces. The large cyclotron effective masses are detected up to 43 m_0 for the field along c-axis.

UTe_2 is one of the hottest materials in the condensed matter physics [1]. It is a heavy fermion paramagnet and gets superconducting below T_c=1.5-2.1K. The huge superconducting upper critical field, H_{c2}, with the field-reentrant behavior resembles those observed in ferromagnetic superconductors, such as URhGe and UCoGe. In ferromagnetic superconductors, strong ferromagnetic fluctuations are developed when the field is applied along the hard-magnetization axis associated with the collapse of the Curie temperature at a high field. On the other hand, UTe_2 has no magnetic order, but the characteristic crossover temperature is linked to the first-order metamagnetic transition at H_m=35T, where the field-reentrant superconductivity is abruptly suppressed. Furthermore, multiple superconducting phases under pressure and at high fields are detected in UTe_2. These unusual superconducting properties are consistent with the spin-triplet state of superconductivity.

In order to clarify the superconducting mechanism, it is important to elucidate the electronic states from a microscopic point of view. Thus, we performed the quantum oscillation measurements, namely the de Haas-van Alphen (dHvA) experiments at high fields up to 30T and at low temperatures down to 30 mK both at Oarai and at Nijmegen, using our ultra-clean samples grown by the liquid-transport molten salt flux method [2,3].

Figure 1 shows the dHvA oscillations and the FFT spectrum. Three fundamental dHvA frequencies, named α_1, α_2, and β are detected. These dHvA frequencies correspond to two kinds of quasi-two-dimensional Fermi surfaces.

Figure 2(a) shows the angular dependence of the dHvA frequencies when the field is tilted from c to a-axis. The experimental results are in good agreement with the theoretical prediction based on the band calculation for 5f-itinerant model of $5f^3$ configuration. The on-site Coulomb repulsion U must be taken into account in the calculation. This may suggest a mixed valence states of U^{3+} and U^{4+} in UTe_2, which is also implied by the field and pressure response of UTe_2.

From the temperature dependence of the dHvA amplitude, we detected the large cyclotron effective masses, which are 43m_0, 39m_0 and 33m_0 for branches α_2, β and α_1, respectively. These large masses indicate the strong correlations of the electronic states, which are responsible for field-robust superconductivity.

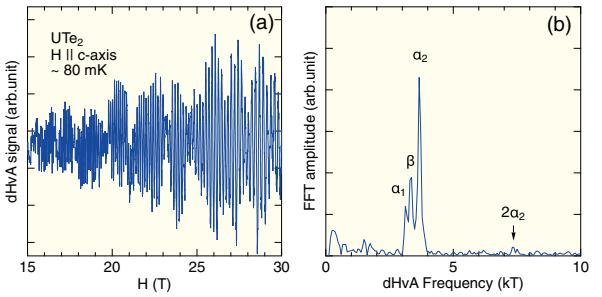

Fig. 1 dHvA oscillations and the corresponding FFT spectrum for the field along c-axis in UTe_2.

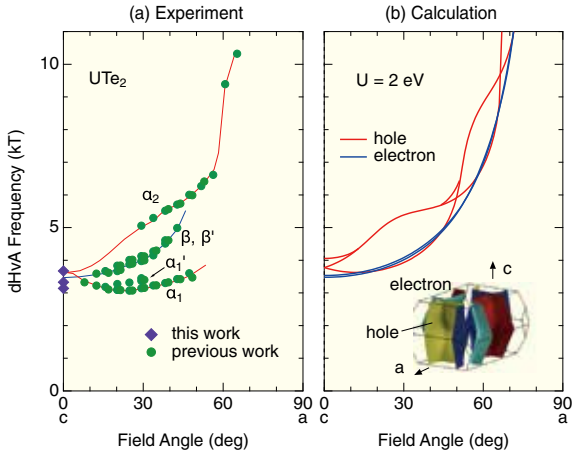

Fig. 2 Angular dependence of the dHvA frequencies from (a) experiments and (b) band calculations in UTe_2. The inset of panel (b) shows the calculated Fermi surfaces.

References

[1] D. Aoki, J. P. Brison, J. Flouquet, K. Ishida, G. Knebel, Y. Tokunaga, and Y. Yanase, J. Phys. Condens. Matter **34**, 243002 (2022).

[2] D. Aoki, H. Sakai, P. Opletal, Y. Tokiwa, J. Ishizuka, Y. Yanase, H. Harima, A. Nakamura, D. Li, Y. Homma, Y. Shimizu, G. Knebel, J. Flouquet, and Y. Haga, J. Phys. Soc. Jpn. **91**, 083704 (2022).

[3] D. Aoki, I. Sheikin, A. McCollam, J. Ishizuka, Y. Yanase, G. Lapertot, J. Flouquet, and G. Knebel, J. Phys. Soc. Jpn. **92**, 065002 (2023).

Dai Aoki (Actinide Materials Science Research Laboratory)
E-mail: dai.aoki.c2@tohoku.ac.jp
URL: http://www.imr.tohoku.ac.jp/en/about/divisions-and-centers/research-division/25.html

Research Centers

IMR KINKEN Research Highlights 2024

GIMRT International Co-Authored Paper

Quasi-One-Dimensional Ferromagnetism with Ising Anisotropy in Single Crystal UNi_4P_2

International Research Center for Nuclear Materials Science

We have successfully grown for the first time single crystals of a ferromagnet UNi_4P_2 using the self-flux technique and performed the magnetization, resistivity, and specific heat measurements. The uniaxial magnetic anisotropy was found not only between a and c-axes, but also in the tetragonal basal plane due to the quasi-one-dimensional crystal structure, revealing the anisotropic electronic correlations.

Uranium compounds attract much attention because of the unusual properties. One of the highlights is coexistence of ferromagnetism and superconductivity discovered in the weak ferromagnets, such as URhGe and UCoGe [1]. The huge and re-entrant upper critical fields, H_{c2}, are detected when the field is applied along the hard-magnetization axis within the Ising-ferromagnetic state. This is due to the strong enhancement of ferromagnetic fluctuations under magnetic fields, which play a crucial role for the spin-triplet states of superconductivity. Recently a heavy fermion paramagnet, UTe_2 was found to be a new candidate for the spin-triplet superconductor [2]. UTe_2 was believed to be an end member of ferromagnetic superconductors associated with strong ferromagnetic fluctuations. However, the mechanism for superconductivity is more complicated than those for ferromagnetic superconductors. In any case, the field-reentrant superconductivity and the multiple superconducting phases give a strong support for spin-triplet superconductivity, which also provides a good playground for studying topological superconductivity.

To search for a new system, we focus on the dimensionality, crystal structure, and Ising ferromagnetism, and choose UNi_4P_2 [3]. As shown in Fig.1(a), the crystal structure is $ZrFe_4Si_2$-type tetragonal with the space group $P4_2/mnm$, which is categorized as non-symmorphic space group, leading to the broken local inversion symmetry. Single crystals were obtained by the self-flux method using a eutectic composition of Ni and P. A large single crystal with the millimeter size was obtained, as shown in Fig.1(b), after centrifuging the flux. Clear Laue spots with four-fold symmetry were detected by X-ray diffraction (see Fig.1(c)).

Figure 2(a) shows the resistivity curves for the different current directions. A clear anisotropy was observed for the current along c-axis and the basal planes. For J ll [100] and [110], a typical heavy fermion-like behavior is observed at high temperatures, but the resistivity rapidly drops on cooling below the Curie temperature, 25K.

Figure 2(b) shows the magnetization curves for H ll [100], [110] and [001] at low temperatures. The anisotropy between c and the basal planes are relatively large, revealing the Ising ferromagnetic properties. From the data for easy-magnetization

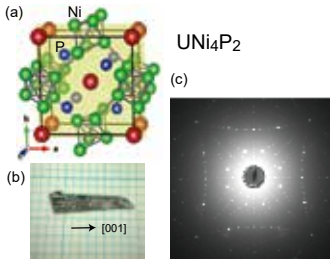

Fig. 1 (a) Tetragonal crystal structure of UNi_4P_2. (b) Single crystal grown by the self-flux method. (c) Laue photograph for c-axis.

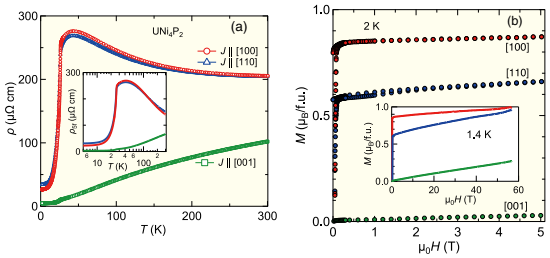

Fig. 2 (a) Resistivity curves for J ll [100], [110] and [001]. (b) Magnetization curves at 2K for H ll [100], [110] and [001]. The inset shows the magnetization curves at 1.4 K with pulse fields up to 55 T.

axis, the ferromagnetic ordered moment is estimated to be ~0.8μB/U, which is much smaller than the expected values for free ion of U $5f^2$ or $5f^3$. The strong anisotropy, however, persists even at very high field up to 55 T. Interestingly, the anisotropy between [100] and [110] also survives at high fields. These unusually strong magnetic anisotropy even in the basal plane may be the consequence of anisotropic electronic correlations and the unique crystal structure.

References

[1] D. Aoki, K. Ishida, and J. Flouquet, J. Phys. Soc. Jpn. **88**, 022001 (2019).
[2] D. Aoki, J. P. Brison, J. Flouquet, K. Ishida, G. Knebel, Y. Tokunaga, and Y. Yanase, J. Phys. Condens. Matter **34**, 243002 (2022).
[3] A. Maurya, A. Miyake, H. Kotegawa, Y. Shimizu, Y. J. Sato, A. Nakamura, D. Li, Y. Homma, F. Honda, M. Tokunaga, and D. Aoki, Phys. Rev. B **107**, 085142 (2023).

Maurya Arvind (Corresponding Author, Mizoram University)
E-mail: amaurya@mzu.edu.in
Dai Aoki (Corresponding Author, Actinide Materials Science Research Laboratory)
E-mail: dai.aoki.c2@tohoku.ac.jp
Yasuyoshi Nagai (Head of International Research Center for Nuclear Materials Science)
E-mail: yasuyoshi.nagai.e2@tohoku.ac.jp
URL: http://www.imr-oarai.jp/en/

GIMRT International Co-Authored Paper

Effect of Helium/Displacement Damage Ratio on Irradiation-Induced Fine Structure Formation in Steels for Fusion Reactors

International Research Center for Nuclear Materials Science

The effect of the ratio of Helium/Displacement per atom (dpa) on irradiation-induced cavities in martensitic steel was investigated with TEM. It is found that a high He/dpa ratio significantly enhances the formation of cavities, which contributes to a better understanding of irradiation-induced fine structures for fusion materials.

Plasma facing materials in fusion reactors are exposed to high-energy neutrons and plasma, resulting in the accumulation of helium atoms and displacement damage. For first-wall materials in commercial fusion reactors, up to 2000 appm of helium and 200 displacements per atom (dpa) are anticipated. This produces a high number density of cavities (helium bubbles and voids), which significantly degrades material properties. The interaction between helium and defects affects the formation and growth of cavities, influenced by the ratio of helium content to displacement damage, He/dpa. Particularly when simulating the neutron irradiation environment in fusion reactors using existing fission reactors, it is essential to consider the impact of the He/dpa ratio on the fine structure formation of materials.

This study aims to elucidate the correlation between the He/dpa ratio and cavity formation in low-activation martensitic steel, which is considered promising as a fusion reactor structural material, through state-of-the-art transmission electron microscopy observations. Significant He/dpa ratio effects on the formation of cavities have been discovered so far [1]. The material used here is low-activation martensitic steel F82H. To simultaneously introduce helium and irradiation defects, helium and iron ions were co-irradiated. Figure 1a provides an overview of TEM observations. When increasing the amount of helium (and dpa) while keeping the He/dpa ratio constant, the size and number density of cavities increased (see Fig. 1b and 1c). On the other hand, even with the same dpa, a smaller He/dpa ratio resulted in a decreased number density of cavities (see Fig. 1c and 1d). Currently, a database including 231 alloys irradiated with simultaneous ion beams up to 3700 appm helium and 82 dpa is available, aiming to provide a model estimating the relationship between He/dpa and the kinetics of cavity formation.

References

[1] T. Yamamoto, Y. Wu, K. Yabuuchi, J. Haley, K. Yoshida, A. Kimura, and G. R. Odette, J. Nucl. Mater. **576**, 154201 (2023).

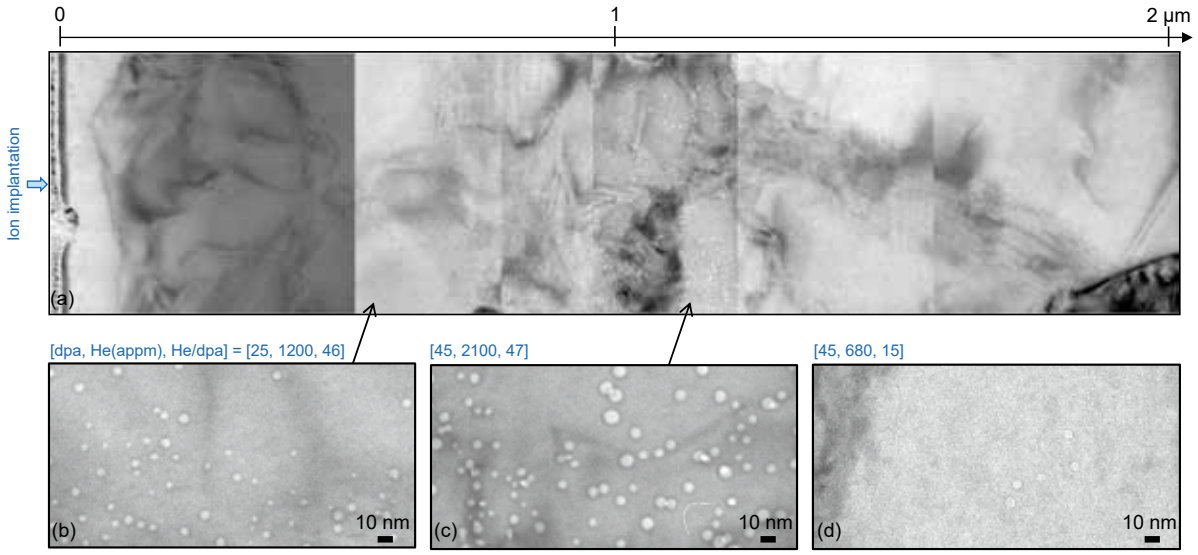

Fig. 1 (a) TEM observation for cavities (helium bubbles and voids) for He- and Fe-ion dual irradiated martensitic steel F82H. (b) Cavities in the region with He/dpa=46 (25 dpa, 1200 appm He). (c) Cavities in the region with He/dpa=47 (45 dpa, 2100 appm He). (d) Cavities in the region with He/dpa=15 (45 dpa, 680 appm He).

Yasuyoshi Nagai (Head of International Research Center for Nuclear Materials Science)
E-mail: yasuyoshi.nagai.e2@tohoku.ac.jp
URL: http://www.imr-oarai.jp/en/

Development of Advanced Alloy Powders by Atmosphere-Controlled Gas Atomization Method

Cooperative Research and Development Center for Advanced Materials

To develop high strength, high thermal and electrical conductivity Cu alloys for fusion reactors, Y, Ti, and Fe, which have lower solid solution limit to Cu than Al and lower oxide standard formation energy, were added to Cu alloys, and their alloy powders were prepared by atmosphere controlled gas atomization method. The microstructure of Cu alloy powder had a typical solidification structure regardless of the alloying elements and gas species, and Fe was in uniform solid-solution in the matrix, while Ti and Y were swept out from the matrix to grain boundaries and particle surfaces during solidification, exhibiting different behavior depending on the additive elements.

The gas atomization method is a process that involves breaking molten metal into small droplets by spraying high-pressure inert gas onto it as a cooling medium, and a clean-surfaced spherical powder can be produced efficiently at a low cost, which exhibits excellent flowability. Therefore, it is commonly used in industry as a method for fabricating raw materials in powder metallurgy and additive manufacturing processes. In addition, by replacing a part of the inert gas with oxygen or nitrogen, fine oxides or nitrides can be precipitated, enabling the development of high-strength materials by precipitation strengthening and grain refinement due to the pinning effect of the precipitates.

Our research group has focused on oxide dispersion strengthened Cu (ODS-Cu) alloys, which have been applied as a coating material for superconducting coils and as a heat sink material for divertors in fusion reactors which are expected to be the next generation energy source, and has being developed a new Cu alloy to replace Gridcop ® (Al_2O_3 dispersion strengthened Cu alloy) that is currently widely available [1]. Cu alloys for fusion reactors are required high strength and high electrical and thermal conductivities, however, there is a trade-off relationship between them. Therefore, Gridcop ®, which has high strength by oxide precipitation strengthening and a composition of the base phase close to pure copper, satisfies these requirements. On the other hand, the solid solution limit of Al against Cu is relatively high, and further functional improvement is possible by selecting appropriate elements. Therefore, we focused on Y, Ti, and Fe, which have a lower solid solution limit against Cu than Al and a lower oxide standard formation energy than Cu, and prepared Cu alloy powders in solid solution with the above elements using a gas atomization method with atmosphere control by using N_2+O_2 mixed gas instead of Ar gas [2].

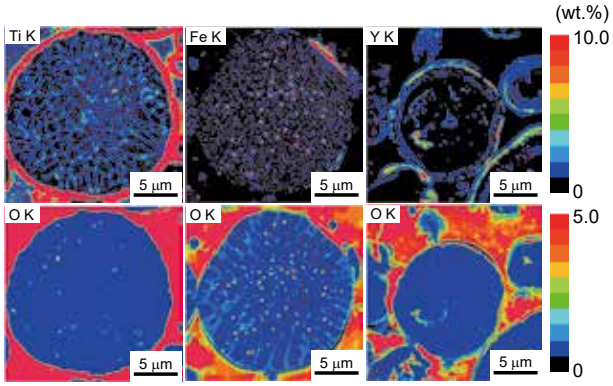

Fig.1 Mapping of additive elements in each alloy particles measured by FE-EPMA.

The microstructures of the obtained alloy powders had a typical solidification structure as seen in cast materials, regardless of the additive elements and gas species.

Figure 1 shows the mapping of each element in the powder prepared using N_2+O_2 gas. Ti and Y were enriched on the grain surface and grain boundaries, while Fe was locally enriched within the grains, exhibiting different behavior depending on the additive elements. On the other hand, O was not only in solid solution in the matrix, but also enriched in the same region as Y, Ti, and Fe, suggesting the formation of oxides.

References

[1] B. Ma and Y. Hishinuma, Fusion Eng. Des. **161**, 112045 (2020).
[2] M. Sato, Y. Shimada, Y. Hishinuma, and N. Masahashi, J. Jpn. Soc. Powder Powder Metall., 23-00017 (2023).

Mitsutaka Sato (Corresponding Author, Cooperative Research and Development Center for Advanced Materials)
E-mail: mitsutaka.sato.a3@tohoku.ac.jp
Hidemi Kato (Head of Cooperative Research and Development Center for Advanced Materials)
E-mail: hidemi.kato.b7@tohoku.ac.jp
URL: http://www.crdam.imr.tohoku.ac.jp/english/

International Co-Authored Paper

Achievement of 25T with a Large-Scale 20-Stacked REBCO Coil for 33T-Cryogen-Free Superconducting Magnet

High Field Laboratory for Superconducting Materials

A large-scale 20-stacked pancake coil with a robust coil structure was fabricated and achieved 24.9 T under a background field of 14 T at 4.2 K with an operating current of 298 A. Both the screening current in REBCO tapes and the coupling current between two-bundled REBCO tapes were observed during ramping up and down and holding the operating current. Optimization of the stress distribution in the REBCO pancake was confirmed as well. This suggests that the robust coil structure works well in a 33-T cryogen-free superconducting magnet.

A 33T cryogen-free superconducting magnet (33T-CSM) is now being developed at HFLSM. It consists of a 19 T $REBa_2Cu_3O_y$ (REBCO, RE; Y, rare-earth elements) insert magnet and a 14 T Nb_3Sn and NbTi Rutherford cable outsert one. The REBCO coated conductor has a high in-field critical current density J_c and good mechanical tolerance but has a risk of local degradation because of a weakness for a delamination. It may give rise to a serious damage in the coil. In order to overcome these risks, we propose the robust REBCO coil structure with two REBCO tape co-winding, all turn separation, and edge impregnation [1]. As one of R&D studies, we fabricated and tested a large-scale 20-stacked REBCO pancake coil with almost the same size of the practical REBCO pancake of the 33T-CSM. We successfully achieved 24.9 T under a background field of 14 T at 4.2 K with an operating current of 298 A as shown in Fig.1 (a) [2]. In addition, two opposite contributions to the magnetic field errors were observed as shown in Fig. 1 (b). The large hysteresis of magnetic field is mainly related to the screening current induced in the REBCO tape width. The relaxation at the magnetic field platou is originated to the coupling current between REBCO tapes. It is found that the effects of the screening current with long time constant and the coupling current with short time constant are compited each other. In addtion, we confirmed that the robust REBCO coil structure can reduce the maximum hoop stress by optimizing stress distribution with a simulation and a strain measurement of the coil [2, 3]. The robustness of the large-scale REBCO coil was also confirmed by the long time operation for about one year with many thermal cycles and shutdown tests.

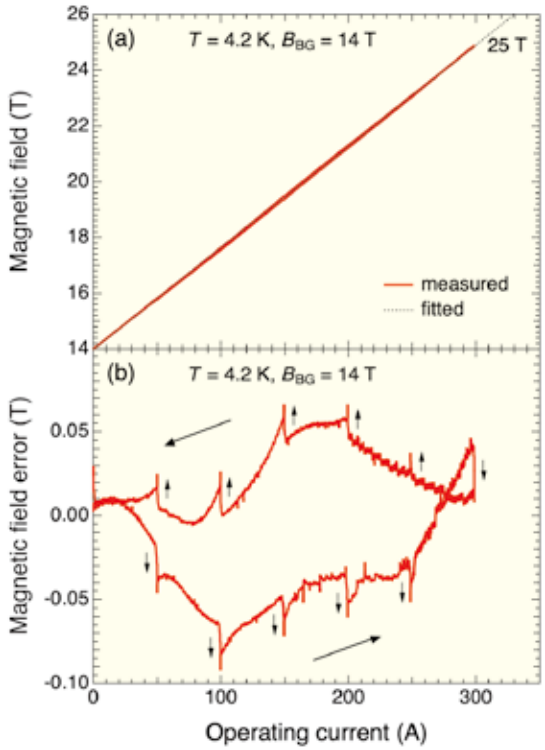

Fig. 1 (a) Magnetic field at the center of 20-stacked coil under a background field of 14 T. (b) Field error, i.e., the difference between the measured value and the fitted linear line as a function of the operating current.

References

[1] S. Awaji, A. Badel, T. Okada, K. Takahashi, H. Miyazaki, S. Hanai, S. Ioka, S. Fujita, S. Muto, Y. Iijima, M. Daibo, and K. Kajikawa, IEEE Trans. Appl. Supercond. **31**, 4300105 (2021).

[2] K. Takahashi, A. Badel, A. Zampa, T. Okada, S. Awaji, G. Nishijima, T. Uto, H. Takewa, S. Hanai, S. Ioka, and J. Inagaki, IEEE Trans. Appl. Supercond. **33**, 4601405 (2023).

[3] A. Badel, K. Takahashi, A. Zampa, T. Okada, G. Nishijima, T. Uto, H. takewa, S. Hanai, S. Ioka, J. Inagaki, and S. Awaji, IEEE Trans. Appl. Supercond. **33**, 4601505 (2023).

Kohki Takahashi (Corresponding Author, High Field Laboratory for Superconducting Materials)
E-mail: kohki.takahashi.e5@tohoku.ac.jp
Satoshi Awaji (Head of High Field Laboratory for Superconducting Materials)
E-mail: satoshi.awaji.e8@tohoku.ac.jp
URL: http://www.hflsm.imr.tohoku.ac.jp/cgi-bin/index-e.cgi

Surface Anisotropic Magnetoresistance in Antiferromagnetic Semiconductor $CrSb_2$

High Field Laboratory for Superconducting Materials

$CrSb_2$ is an antiferromagnetic narrow-gap semiconductor with a metallic surface state. Although the bulk antiferromagnetic state is well understood, the magnetic properties of the surface state are elusive. Here, we perform the low-temperature angle-dependent magnetoresistance measurements up to 24 T and reveal that $CrSb_2$ has an antiferromagnetic surface state with a strong spin-orbit interaction.

A narrow-gap semiconductor $CrSb_2$ is a sister compound of $FeSb_2$, a topological Kondo insulator candidate. Although the resistivity of conventional semiconductors diverges as the temperature approaches zero, $CrSb_2$ and $FeSb_2$ exhibit a resistivity plateau below ~10 K, suggesting the presence of metallic surface states. While $FeSb_2$ and other topological materials with topological surface states are non-magnetic, it is interesting that $CrSb_2$ shows a collinear antiferromagnetic order at 273 K. This magnetic bulk state leads us to expect that the $CrSb_2$ surface state is also magnetic. If so, such magnetic surface states are not expected in topological insulators, and $CrSb_2$ is thereby a unique compound in condensed matter physics and spintronics. To unveil the physics of the $CrSb_2$ surface state, we have performed the angle-dependent magnetoresistance (ADMR) measurements at low temperatures and in high magnetic fields up to 24 T with 25T-CSM at HFLSM, IMR, Tohoku University [1].

The largest plane of the $CrSb_2$ single crystal sample is the *ac* plane [Fig. 1(a)]; on this plane, the surface state was reported previously. ADMR was measured at low temperatures for three rotational directions [α, β, and Υ scans in Fig. 1(b)].

Figure 1(c) shows the ADMR data of the α, β, and Υ scans measured at 24 T and 1.4 K. At this temperature, the conductivity of the bulk state is several orders of magnitude smaller than that of the surface state; thus, the observed ADMR is safely ascribed to the signals from the surface state. As shown in Fig. 1(c), ADMR shows clear twofold symmetry for α, β, and Υ scans. Our numerical calculation shows that the observed ADMR is consistent with the anisotropic magnetoresistance (AMR) due to the slight change in the antiparallel magnetic structure caused by the magnetic field. The $CrSb_2$ surface state is indeed antiferromagnetic, and surface AMR was successfully observed.

In zero magnetic field, the collinear antiferromagnetic moments are aligned along the easy axis and tilted by 61.5 deg. from the *x-axis* [Fig. 1(a)]. The exchange interaction and uniaxial anisotropy are so strong that the antiferromagnetic moments are only tilted slightly (~2%) and hardly rotated even at 24 T. Nevertheless, the large AMR is surprisingly observed. The magnitude of AMR reaches 9.3%, comparable to that reported for ferromagnetic materials.

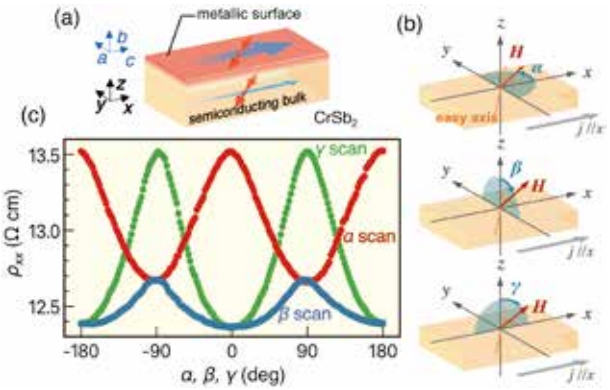

Fig. 1 (a) Schematic illustration of bulk and surface states of $CrSb_2$.The surface state is illustrated only on the top surface for simplicity. The relation between *x*, *y*, and *z*-axes and crystallographic *a*, *b*, and *c*-axes are also illustrated. The direction of electric current is represented by blue arrows and that of antiferromagnetic moments by red arrows. The magnetic easy axis lies in the *xy* plane and is tilted by 61.5 deg. from the *x*-axis. (b) Sketches of the definition of angles α, β, γ and the measurement configuration of angle-dependent magnetoresistance (ADMR). (c) ADMR results of α, β and γ scans measured at 24 T and 1.4 K.

The sizable magnitude of the surface AMR, up to 9.3%, indicates that the surface state of $CrSb_2$ not only has an antiferromagnetic order but also a strong spin-orbit interaction. Such exotic magnetic surface states could be useful in the emerging field of antiferromagnetic spintronics.

References

[1] K. Nakagawa, M. Kimata, T. Yokouchi, and Y. Shiomi, Phys. Rev. B **107**, L180405 (2023).

Yuki Shiomi (Corresponding Author, The University of Tokyo)
E-mail: yukishiomi@g.ecc.u-tokyo.ac.jp
Satoshi Awaji (Head of High Field Laboratory for Superconducting Materials)
E-mail: satoshi.awaji.e8@tohoku.ac.jp
URL: http://www.hflsm.imr.tohoku.ac.jp/cgi-bin/index-e.cgi

Scientific Breakthrough Toward Creation of New Industrial Materials

Trans-Regional Corporation Center for Industrial Materials Research

The institute for Materials Research (IMR) has launched the Trans-Regional Corporation Center, a comprehensive IMR-wide effort that pairs IMR's research groups across the innovation spectrum to solve current industrial challenges and transform the future global energy problems. The center was established in 2016 based on an agreement between IMR, the Osaka Prefecture Government, and enterprises sponsored by the government, and took control of the Osaka and Kansai center projects.

The Center was established in Osaka as a special unit in 2016 based on an agreement with the Osaka Prefecture Government, aiming to solve technical problems that industries have struggled to resolve, to introduce academic output to industries, and to educate next-generation materials scientists and researchers in industries. Projects are conducted through collaborations between the government, universities, research institutions, and other organizations. The Center has four venues: the Osaka office at Osaka Prefecture University, the Hyogo office at University of Hyogo, the Sendai office, and MOBIO in Higashi-Osaka in Osaka Prefecture.

The Center has developed various materials and process technology under collaboration with industries and universities. One of them is to develop a bioactive newly-developed TiNbSn (TNS) alloy [1]. Figure 1 shows (a, c) TEM microphotos and (b, d) EDX line scans of the anodized (a, b) TNS and (c, d) Ti, showing that the oxide on TNS with rutile TiO_2 was 1.3 μm thick and contained homogeneously distributed pores. In contrast, the anodized Ti exhibits anatase TiO_2 with a pore-rich layer parallel to the oxide-substrate interface, and the oxide thickness was approximately 0.3 μm. Figure 2 shows the OCP variations during the fretting tests of anodized (a) TNS and (b) Ti with untreated samples. It reveals that the OCP dropped to negative direction in the untreated samples and anodized Ti, but not in the anodized TNS. The OCP drop is attributed to depassivation. Free of negative shift in the anodized TNS is due to a hard, adherent, and corrosion-resistant TiO_2. This study revealed the anodized TiNbSn exhibits the superior tribocorrosion properties, and the results correlated well with the microstructure and mechanical properties of the anodic oxide. Similar collaboration researches have been in progress. The Center will make an effort to innovate the metallic material industry through the alliance with the partners, and promote scientific research in materials science.

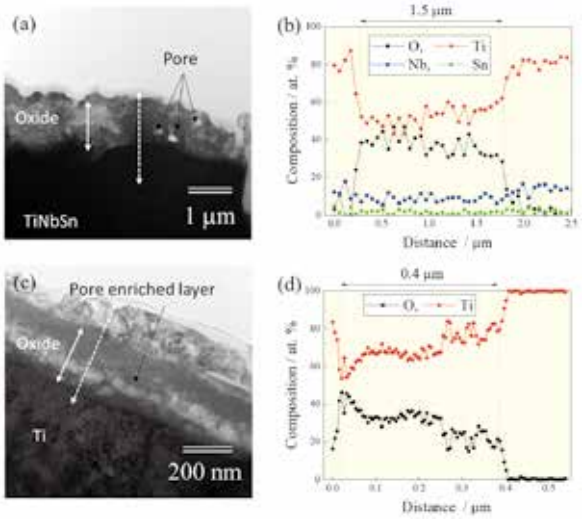

Fig. 1 (a, c) TEM images and (b, d) EDX scans of the anodic oxides on (a, b) TiNbSn and (c, d) Ti.

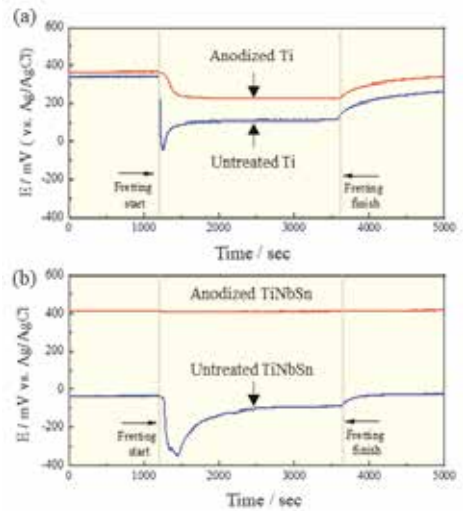

Fig. 2 OCP variations during the fretting wear tests for anodized (a) Ti and (b) TiNbSn alloy with untreated samples.

References

[1] M. Kubota, N. Masahashi, H. Inoue, Y. Michiyama, K. Ohmura, and S. Hanada, Surf. Coat. Technol. **462**, 129492 (2023).

Naoya Masahashi (Head of Trans-Regional Corporation Center for Industrial Materials Research)
E-mail: naoya masahashi.e6@ tohoku.ac.jp
URL: http://www.imr.tohoku.ac.jp/en/about/divisions-and-centers/facilities/04.html

GIMRT International Co-Authored Paper

International Joint Research on Energy Materials

Collaborative Research Center on Energy Materials

International collaborations are carried out in each unit of E-IMR, and this report introduces the international joint research being conducted in the Solar Energy Unit.

1. Silicon crystal growth for solar cells

Silicon (Si) crystalline materials are the most important material, accounting for more than 90% of the world's practical solar cells production. To further improve the energy conversion efficiency of solar cells, it is necessary to improve the quality of the Si crystals, which requires a fundamental understanding of the various phenomena that occur during the solidification process.

The solar cell unit of E-IMR is conducting an international collaboration with Dr. Nathalie Mangelinck-Noël's group at IM2NP, Aix-Marseille University (France) and Prof. Thierry Duffar at Grenoble Institute of Technology (France), to elucidate crystal growth mechanisms of Si. In E-IMR, solid-liquid interface phenomena during Si crystal growth are observed in-situ by optical methods. In IM2NP, that is also observed in-situ by X-ray imaging method at the European Synchrotron Radiation Facility (ESRF). Prof. Duffar has been studying the crystal growth mechanism theoretically and analytically. The objectives of these groups are in perfect agreement and a good collaboration has been established.

To date, some experimental results by in-situ observations obtained at E-IMR have been shared with Prof. Duffar, and the kinetics at solid-liquid interface of Si have been analyzed [1]. In May of this year, Prof. Fujiwara (E-IMR) participated in a 10-day Si solidification experiments of IM2NP at ESRF. And in November of this year, Dr. Mangelinck-Noël visited E-IMR and introduced their research at the E-IMR seminar (Fig. 1).

We are planning to conduct more collaborative experiments between E-IMR and IM2NP researchers, including students, next year.

Fig. 1 Dr. Mangelinck-Noël speaks at the E-IMR seminar.

Fig. 2 Fabrication of half-Heusler alloys at IMR.

2. Research on new thermoelectric materials

Half Heusler (HH) alloys with general formula XYZ can be recognized as excellent thermoelectric candidates. A collaboration was then initiated between SSN Institutions (India) and the solar energy unit of E-IMR through the GIMRT joint research project to search for and realize new half-Heusler alloys with superior performance indice, *ZT*.

Theoretical analyses showed that ZrMnSi and HfMnSi are half metals having band gap in spin down channel with the band gap energy 1.268 eV and 1.311 eV, respectively [2]. Also, it was indicated that the maximum *ZT* values of ZrMnSi and HfMnSi are 0.46 and 0.31 at 1200K, respectively [2]. Therefore, these materials could potentially be used as thermoelectric materials. Dr. Srinivasan and a PhD student (SSN Institutions) stayed at E-IMR and experimentally fabricated some new half-Heusler materials with Ms. Nomura (Cooperative Research and Development Center for Advanced Materials; CRDAM) and Prof. Okamoto (E-IMR), as in Fig. 2. Those samples are being characterized in SSN Institutions. This collaboration will be continued in the future.

References

[1] T. S. S. Mishra, L.-C. Chang, K. Maeda, J. Nozawa, H. Morito, T. Duffar, and K. Fujiwara, J. Crystal Growth **627**, 127524 (2024).

[2] D. Shobana Priyanka, J. B. Sudharsan, M. Seinivasan, N. Elavarasan, P. Ramasamy, and K. Fujiwara, J. Magnetism and Magnetic Materials **588**, 171409 (2023).

Kozo Fujiwara (Corresponding Author, Collaborative Research Center on Energy Materials)
E-mail: kozo.fujiwara.c6@tohoku.ac.jp
Tetsu Ichitsubo (Head of Collaborative Research Center on Energy Materials)
E-mail: tichi @tohoku.ac.jp
URL: http://www.imr.tohoku.ac.jp/en/about/divisions-and-centers/facilities/05.html

GIMRT

All-Electron *GW* Approach for Light-Element-Doped Anatase TiO_2

Center for Computational Materials Science

All-electron *GW* approach based on the many-body perturbation theory was adopted to determine the electronic structures and understand the mechanism of band gap narrowing for anatase TiO_2 doped with light elements (such as C and N) and its various defect states. It is clearly shown that the band gap could be controlled by the oxygen pressure and doping states, and C, N codoping narrowed the band gap more than monodoping.

TiO_2 is known as a photocatalytic material, and its band gap corresponds to the UV region. Adding visible-light responsive photocatalytic functionality to TiO_2 by doping of impurity elements such as C and N could promote its technological applicability. An example is the TiO_2 coating on Ti dental implants to achieve antibacterial properties, which are induced by its photocatalytic reactions.

In this study, we determine the electronic structures of C- and N-doped anatase TiO_2. To do this, we first construct various models of C and N monodoped and codoped TiO_2 considering the oxygen vacancy(ies) and estimate the stable models through formation energy analysis as a function of the oxygen (O_2) pressure or oxygen chemical potential. Then, for the stable models, *GW* calculations using the all-electron mixed basis approach are performed to analyze the electronic structures and clarify the mechanism of band gap narrowing that originates because of impurity doping. Finally, we discuss a possible way to realize an oxygen pressure condition under which visible-light response TiO_2 can be synthesized.

The *GW* method has been implemented in the TOhoku Mixed Basis Orbitals ab initio program (TOMBO) [1]. TOMBO uses the all-electron mixed basis approach, in which the electronic wave function is expressed by a linear combination of plane waves and atomic orbitals.

The stability of the C- and N-doped models varies depending on the oxygen pressure conditions. Furthermore, the all-electron *GW* calculations indicate that the band gaps of the C- and N-doped models are found to be narrowed primarily owing to impurity levels introduced in the gap. Figure 1 (a) summarizes the stable models and their band gaps as functions of the oxygen pressure at 700K or oxygen chemical potential. It is shown that the band gaps vary by up to 1 eV and that codoping with C and N is more effective for narrowing the band gap when compared with monodoping.

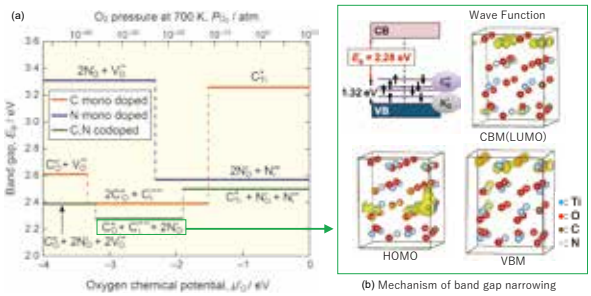

Fig. 1 (a) Relationship between the band gap and oxygen pressure (or oxygen chemical potential) for C- and N-doped anatase TiO_2, and (b) Mechanism of band gap narrowing for the $C_O^{\cdot\cdot} + C_i^{\bullet\bullet\bullet\bullet} + 2N_O^{\cdot}$ model.

Among the stably doped models identified in this study, the $C_O^{\cdot\cdot} + C_i^{\bullet\bullet\bullet\bullet} + 2N_O^{\cdot}$ model under the medium oxygen pressure condition exhibited the smallest band gap (2.28 eV).

Figure 1(b) shows the mechanism of band gap narrowing for the $C_O^{\cdot\cdot} + C_i^{\bullet\bullet\bullet\bullet} + 2N_O^{\cdot}$ model. The band structure shows that the occupied impurity levels derived from $C_O^{\cdot\cdot}$ and $N_O^{\cdot}$ in the gap led to a narrowing of the band gap. Selected wave functions of CBM (conduction band minimum), HOMO (highest occupied molecular orbital), and VBM (valence band maximum) are also shown.

A possible means to synthesize TiO_2 could be the thermal oxidation of Ti in the gas mixture of CO-CO_2-N_2 under intermediate oxygen pressure conditions, which suggests that visible light photocatalytic materials based on anatase TiO_2, could be manufactured through C and N codoping [2].

References

[1] S. Ono, Y. Noguchi, R. Sahara, Y. Kawazoe, and K. Ohno, Comput. Phys. Commun. **189**, 20 (2015).

[2] T. Ishikawa, R. Sahara, K. Ohno, K. Ueda, and T. Narushima, Comput. Mater. Sci. **220**, 112059 (2023).

Ryoji Sahara (Corresponding Author, National Institute for Materials Science)
E-mail: SAHARA.Ryoji@nims.go.jp
Momoji Kubo (Head of Center for Computational Materials Science)
E-mail: momoji@tohoku.ac.jp
URL: https://www.sc.imr.tohoku.ac.jp/eng/

GIMRT International Co-Authored Paper

Current Status of Collaborative Research Programs of CNSAM

Center of Neutron Science for Advanced Materials

The Center of Neutron Science for Advanced Materials is a neutron facility which has a background of novel materials science in IMR. This center manages four neutron instruments at the research reactor facility JRR-3 and spallation neutron sauce J-PARC MLF. Here, we report the current status of the research program and the outcome obtained from JRR-3, which started the reoperation in 2021.

The Center of Neutron Science for Advanced Materials (CNSAM) was established in 2010 to promote novel materials science research using neutrons. CNSAM operates one diffractometer (HERMES) and two neutron spectrometers (TOPAN and AKANE) at the JRR-3 research reactor of the Japan Atomic Energy Agency. HERMES can determine the arrangement of atoms and spins, while their motions are examined by AKANE and TOPAN. POLANO, located at the Materials and Life Science Experimental Facility (MLF) at the Japan Proton Accelerator Research Complex (J-PARC), is a spectrometer designed to perform polarization analysis in higher energy regions. We aim to contribute to condensed matter physics and materials science with the multipurpose neutron instruments of PATH, which is a collective term for neutron instruments managed by the CNSAM.

To achieve this purpose, we established an international collaborative research program in IMR from FY 2019. We provide opportunities not only for experiments with neutron beams but also for the development of neutron devices and analysis methods, and even for theoretical work with our neutron data. Proposals can be submitted under several categories, such as “Neutron experiment at MLF/JRR-3,” “Instrumental development,” “Development in analysis method,” and “Structural analysis and data handling”. In FY 2023, we received 33 and 9 proposals from domestic and overseas researchers, respectively. Furthermore, the research reactor JRR-3 started the reoperation in February 2021, and we received 39 proposals for our neutron instrument at JRR-3 through the user program managed by the Institute for Solid State Physics, the University of Tokyo. The number of proposals is increasing year by year. The number of proposals in FY 2023 is more than doubled of that in FY 2019, and the ratio of accepted international proposal is over 20% of the total number. The results obtained with our instruments have led to publication in high impact factor journals [1, 2]. In this way, the activities of center are revitalizing the use of neutron beams in Japan.

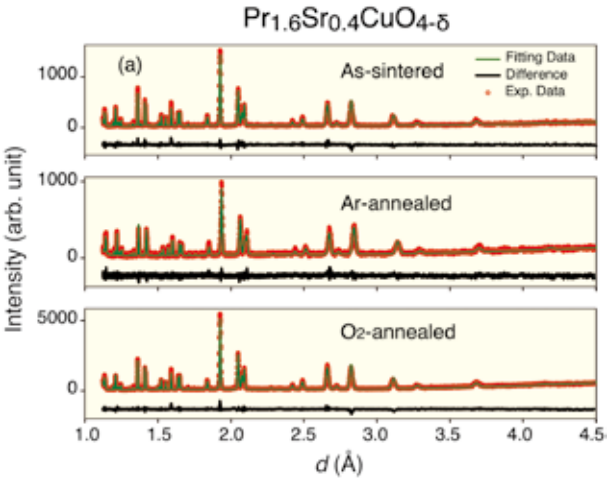

Fig. 1 Neutron powder diffraction pattern of (a) as-sintered, (b) Ar-annealed, and (c) O_2-annealed $Pr_{1.6}Sr_{0.4}CuO_{4-\delta}$.

Here, we introduce an example of obtained results from HERMES [3]. Figure 1 shows the neutron powder diffraction pattern of as-sintered, Ar-annealed and O_2-annealed $Pr_{1.6}Sr_{0.4}CuO_{4-\delta}$ (PSCO). By the Rietveld analysis, it was clarified that the *c*-axis elongates (shrinks) due to Ar-annealing (O_2-annealing). This trend is opposite to the annealing effect on the *c*-lattice constant in other cuprate oxides. Thus, PSCO provide unique opportunity to study the physical properties and the crystal structure.

References

[1] R. Morikawa, T. Murakami, K. Fujii, M. Avdeev, Y. Ikeda, Y. Nambu, and M. Yashima, Commun. Mater. **4**, 42 (2023).

[2] Y. Sakuda, T. Murakami, M. Avdeev, K. Fujii, Y. Yasui, J. R. Hester, M. Hagihara, Y. Ikeda, Y. Nambu, and M. Yashima, Chem. Mater. **35**, 9774 (2023).

[3] T. Wang, P. Xie, T. Taniguchi, and M. Fujita, JPS Conf. Proc. **38**, 011043 (2023).

Masaki Fujita (Head of Center of Neutron Science for Advanced Materials)
E-mail: fujita@tohoku.ac.jp
URL: http://nc-imr.imr.tohoku.ac.jp/index-e.html, http://qblab.imr.tohoku.ac.jp

Guest Induced Spin-State Switching in Hoffmann-Type Coordination Polymers

International Collaboration Center

The reversible interconversion between the high-spin (HS) and low-spin (LS) states in transition metal complexes is being studied in the presence of different stimuli. The advantage of the porous Hoffmann-type framework is that the adsorption and desorption of gas molecules can play an important role in switching the spin state. In this project, the CO_2-induced gate opening, and spin-crossover behavior were observed for the first time in the Hoffmann framework.

Traditionally, for a flexible porous crystal, the *"breathing effect" is demonstrated by* a drastic expansion/contraction in the pore volume upon increasing the partial pressure. Needless to mention that the extreme sensitivity of the spin crossover (SCO) property to minute structural changes and host-guest interactions imposes a formidable challenge in designing the guest responsive porous magnetic materials [1]. In that context, the Hofmann-type coordination polymers (HCPs) are of great interest, as the polymeric network exhibits stronger cooperativity between the SCO sites linked through covalent bonds to create a rigid lattice.

Inspired by our earlier demonstration [2] of single-to-four-step spin transition by de/re-solvation of MeOH molecules in a 2D Hoffmann-type coordination polymer $[Fe^{II}Pd(CN)_4L_2]\cdot 1.3MeOH$ (**1**·1.3MeOH**,** L = methyl isonicotinate), we sought to rationalize the system under the effect of a supercritical gas, like CO_2, which could only impart weak dispersive interactions in the system. Notably, removing MeOH molecules from **1** exerts stronger π-stacking interactions between the paneling ligands, which leads to the intriguing gate-opening/closing mechanism.

In this collaborative project with the Miyasaka group, we report the first case of a CO_2-gated reversible spin-state switching in an interdigitated Hofmann-type coordination polymer(**1**) showing a wide range of temperature (T_{eq}) shift from ~150 K at P_{CO2} = 0 kPa to ~250 K at P_{CO2} = 100 kPa. Interestingly, the emergence of a stepped behavior below P_{CO2} = 10 kPa, and overlapping magnetic susceptibility values with no change in the transition temperature (T_H) above P_{CO2} = 10 kPa elucidate the selective stabilization of the LS state under the influence of the CO_2 atmosphere. Based on the magnetic response, and the phase transition diagram obtained under the respective P_{CO2}, a plausible scenario of the spin-state switching can be interpreted as $1_{LS} \rightarrow (1_{LS} + 1'_{LS}) \rightarrow (1_{HS} + 1'_{LS}) \rightarrow 1'_{HS} \rightarrow 1_{HS}$, where the CO_2-free and CO_2- encapsulated states are represented as 1, and 1', respectively. The magnetic sensitivity based on the varied external CO_2 pressure corroborates a novel and intriguing case for the development of CO_2- responsive magnets henceforth.

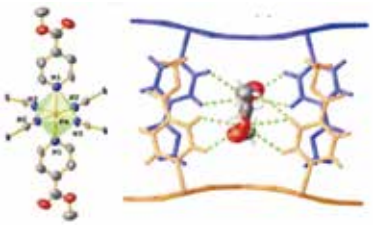

Fig. 1 Asymmetric unit of $[Fe^{II}(L)_2Pd(CN)_4]\cdot 1.3MeOH$ (L = methyl isonicotinate), and position solvent molecules in between the layers.

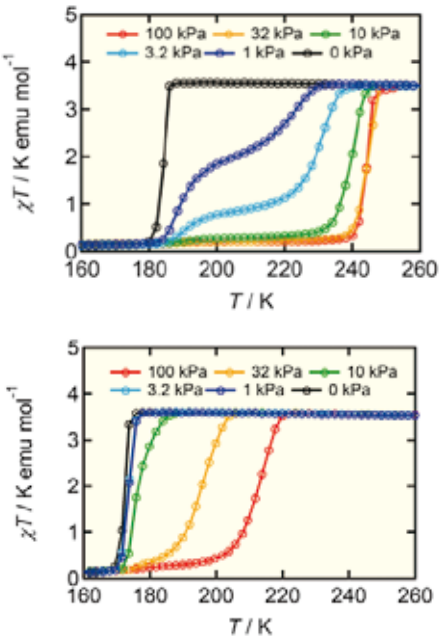

Fig. 2 The CO_2 pressure dependence of the magnetic susceptibility measurements in cooling(top) and (c) heating mode(bottom).

References

[1] W. Kosaka, H. Nemoto, K. Nagano, S. Kawaguchi, K. Sugimoto, and H. Miyasaka, Chem. Sci. **14**, 791 (2023).

[2] D. J. Mondal, A. Mondal, A. Paul, and S. Konar, Inorg. Chem. **61**, 4572 (2022).

Sanjit Konar (Corresponding Author, International Collaborative Center)
E-mail: skonar@iiserb.ac.in
Hiroyuki Nojiri (Head of International Collaborative Center)
E-mail: icc-imr@grp.tohoku.ac.jp
URL: http://www.icc-imr.imr.tohoku.ac.jp/

Li-Intercalation into Santabarbaraite

Center for Advanced Light Source and Materials Science

This study focused on unique cation intercalation process induced by the dehydration and deprotonation of hydrous minerals. Li-intercalation on hydrous phosphate mineral of santabarbaraite was studied, and this mineral indicates a superior capacity of Li^+ compared to the partially-oxidized parent vivianite. The difference in Li^+ capacity is owing to the total amount of Fe^{3+} derived from oxidation progress at low temperatures. The reaction rate of Li-intercalation of santabarbaraite was significantly encouraged by the interstitial space caused by the unique dehydration process of parent vivianite [1].

Santabarbaraite is a mineral produced by the dehydration and deprotonation of vivianite. XANES spectra of various santabarbaraite samples are shown in Fig 1. A spectrum of 500 °C heated santabarbaraite is shown to compare the oxidation state of Fe with that of 120 °C heated one. Fe *K*–absorption edge of phosphophyllite and vivianite with Fe^{2+} are around 7120 eV and the absorption edge shift could be readily observed between as synthesized vivianite and 120 °C heated santabarbaraite. On the other hand, there was no significant sign of the oxidation progress between the 120 °C heated and 500 °C heated santabarbaraite.

Li-intercalation performance was tested by observing the CC-CV discharging process with vivianite- or santabarbaraite-electrode.

The total amount of intercalated Li^+ of the santabarbaraite-electrode was about two times larger than that of the vivianite-electrode (156 and 70.9 $mAhg^{-1}$ for santabarbaraite and vivianite, respectively). This is because the total amount of Fe^{3+} of santabarbaraite is larger than that of vivianite.

It should be noted that the santabarbaraite-electrodes indicate a significantly high reaction rate of Li-intercalation in comparison with that of vivianite. These features are well attributed to the active space for Li+ diffusivity, probably produced by the dehydration and deprotonation process of vivianite.

Additionally, the accumulated amount of Li^+ in vivianite- or santabarbaraite-electrode was evaluated from both the electrochemical measurement and ICP-AES analysis. Both evaluations show consistent results each other, and santabarbaraite can accumulate Li^+ about 80 % compared to the number of Fe ions. This result suggests that 80% of the Fe is in the trivalent Fe^{3+} state in santabarbaraite heated to 120 °C, and is consistent with the results of XANES measurements, which indicate that the oxidation progress of santabarbaraite is almost complete at 120 °C.

Figure 2 shows the XRD patterns of the santabarbaraite heated to 120 °C before and after Li intercalation. A

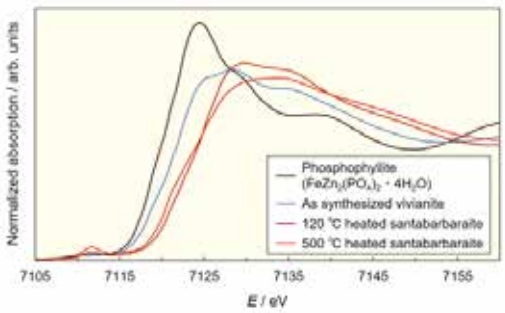

Fig. 1 XANES spectra of as synthesized vivianite and heated santabarbaraite together with phosphophyllite.

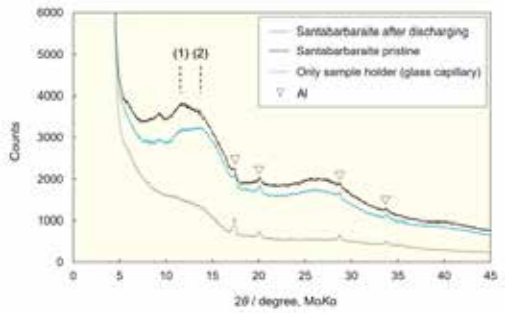

Fig. 2 XRD patterns of the 120 °C heated santabarbaraite before/ after the Li-intercalation.

characteristic change was observed around the 2θ region of 10-15°. The relative intensity profile at about 2θ = 12° with the corresponding distance of 4.5 Å was strongly modified by the Li intercalation. This correlation length corresponds to the in-plane structure of the 2D $Fe_3(PO_4)_2$ sheet in the parent vivianite. Since a similar change could also be observed in the diffraction profile after the Li intercalation of the crystalline vivianite, the Li+ intercalation in santabarbaraite, as in vivianite, induces a disorder in the atomic arrangements in the 2D-$Fe_3(PO_4)_2$ sheets.

References

[1] R. Yamane, H. Li, T. Ichitsubo, and K. Sugiyama, Phys. Chem. Chem. Phys. **25**, 31346 (2023).

Ryo Yamane (Corresponding Author, Chemical Physics of Non-Crystalline Materials Research Laboratory)
E-mail: ryo.yamane.c2@tohoku.ac.jp
Kazumasa Sugiyama (Head of Center for Advanced Light Source and Materials Science)
E-mail: kazumasa.sugiyama.e6@tohoku.ac.jp
URL: https://www.imr.tohoku.ac.jp/en/about/divisions-and-centers/collaboration/08.html

Geometrical Frustration Originated from Magnetic Quadrupole Interactions of the RKKY Mechanism on a Breathing Kogome Lattice

Laboratory of Low Temperature Materials Science

We studied frustrated spin system $Gd_3Ru_4Al_{12}$ with a breathing Kagome lattice structure. This compound is known as one of host materials of skyrmion [1]. We determined anisotropic magnetic phase diagrams of $Gd_3Ru_4Al_{12}$, and revealed that easy axis and easy plane types of magnetic anisotropies coexist in this spin system. These anisotropies are originated from magnetic quadrupole (MQ) interactions of the RKKY mechanism.

In frustrated spin system $Gd_3Ru_4Al_{12}$, ferromagnetic (FM) Gd-trimers are formed below 184 K on the small triangles with decreasing temperatures [2]. These FM trimers form an antiferromagnetic (AFM) triangular lattice (Fig. 1).

We have determined magnetic phase diagrams of $Gd_3Ru_{-4}Al_{12}$ by specific heat and magnetic measurements [3]. The diagrams show clear anisotropies, which can be understood as a simple superposition of easy axis (e. a.) and easy plane (e. p.) types of AFM phase diagrams (Fig. 2). We revealed that the imperfect FM trimers possess MQ moments and that the MQ interactions of the RKKY mechanisms lead to magnetic anisotropies. In ordered states, two kinds of spontaneous MQ moments appear to reduce frustration among MQ moments, and the spin system splits into two sub-systems which approximately do not interact with each other in a quadrupole manner. This separation results in the coexistence of the different magnetic anisotropies depending on the sites of the trimers [3].

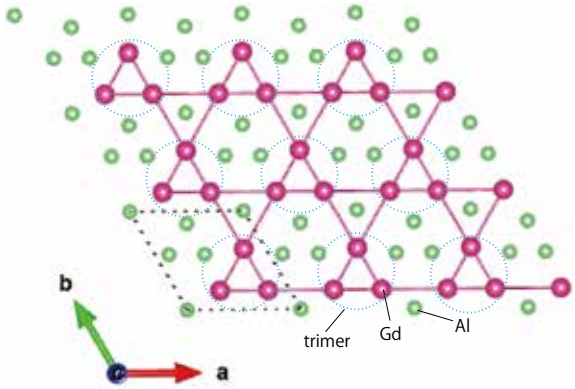

Fig. 1 The breathing kagome structure on the Gd-Al plane of $Gd_3Ru_4Al_{12}$.

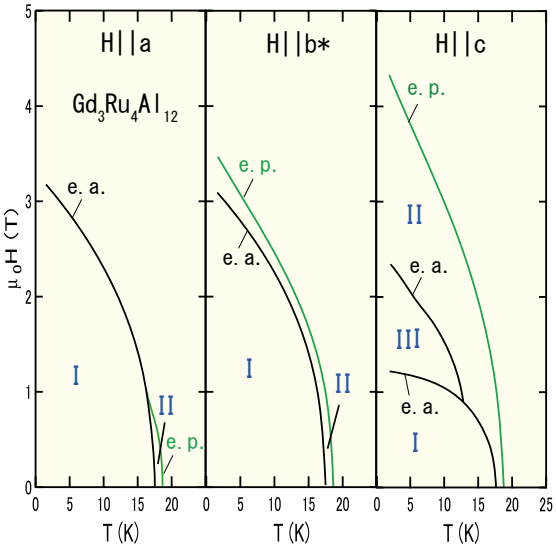

Fig. 2 Schematic magnetic phase diagrams of $Gd_3Ru_4Al_{12}$.

References

[1] M. Hirschberger, T. Nakajima, S. Gao, L. Peng, A. Kikkawa, T. Kurumaji, M. Kriener, Y. Yamasaki, H. Sagayama, H. Nakao, K. Ohishi, K. Kakurai, Y. Taguchi, X. Yu, T. Arima, and Y. Tokura, Nat. Commun. **10**, 5831 (2019).

[2] S. Nakamura, N. Kabeya, M. Kobayashi, K. Araki, K. Katoh, and A. Ochiai, Phys. Rev. B **98**, 054410 (2018).

[3] S. Nakamura, N. Kabeya, M. Kobayashi, K. Araki, K. Katoh, and A. Ochiai, Phys. Rev. B **107**, 014422 (2023).

Shintaro Nakamura (Corresponding Author, Laboratory of Low Temperature Material Science)
E-mail: shintaro.nakamura.c8@tohoku.ac.jp
Takahiko Sasaki (Head of Laboratory of Low Temperature Material Science)
E-mail: takahiko.sasaki.d3@tohoku.ac.jp
URL: http://ltsd.imr.tohoku.ac.jp

Research Facility for Physics and Chemistry of Radioactive and Nuclear Materials

Laboratory of Alpha-Ray Emitters

More than 190 species of radioisotopes and nuclear materials are available for study at the Laboratory of Alpha-Ray Emitters. This laboratory is one of the most important centers worldwide for studying the physical and chemical properties of radioactive materials such as actinide compounds. Researchers from many leading universities and institutes all over Japan visit this facility every year to prepare a variety of materials and conduct chemical and physical experiments.

The Laboratory of Alpha-Ray Emitters provides a research environment for the study of 190 radionuclides and elements, especially alpha-ray emitters, such as actinide. This lab functions as a source for the preparation of pure crystals of actinide compounds, providing them to other universities and to synchrotron particle accelerators. In the past decade, actinium-225 (Ac-225), one of the actinides, has been provided as an inter-university collaboration to other universities and research centers. The radiation-controlled area of this laboratory includes three chemical rooms, three physical rooms, and other facilities that are equipped with local exhaust ventilation systems, making the handling of various kinds of radioactive material possible. Many spectrometers, including those for gamma rays and alpha rays, are available.

The past two decades have witnessed a revival of interest in low-valent uranium chemistry such as the unusual reactions mediated by uranium [1]. As further development in this field relies on the availability of U(III) starting materials such as halides and triflate (OTf), the establishment of their convenient syntheses has drawn much attention.

U(III) species (e.g., UI_3 and $U(OTf)_3$) and their solvent adducts are typically prepared from U metal, while other routes such as the reduction of U(IV) by metals or other agents are less common, because of the difficulty of separating the spent reducing agent from U(III) products. Recently, to shed light on the electrochemical behavior of U(IV) triflate, we probed the electrode reactions of $U(OTf)_4$ in DMF containing tetrabutylammonium triflate (TBAOTf) as a supporting electrolyte by voltammetry, using the standard hanging mercury electrode (HME) and that where Hg was substituted by Zn(Hg). For comparison, we also probed the bulk electrolysis of $U(OTf)_4$ in the presence of Zn(II) in DMF containing TBAOTf on both the pool Hg and the Zn(Hg) electrode. The electroseparation of Zn(II) from the U(III) solution prepared by the reduction of $U(OTf)_4$ on Zn(Hg) in DMF was studied (Fig. 1) for the first time to evaluate the possibility of the convenient preparation of spent reductant-free U(III) starting materials [2]. Here, we successfully electroseparated Zn(II) from the U(III) solution on Zn(Hg) (highest coulombic efficiency = 0.81, final Zn(II) separation ratio = 93.4%) after the reduction of $U(OTf)_4$ by Zn(Hg).

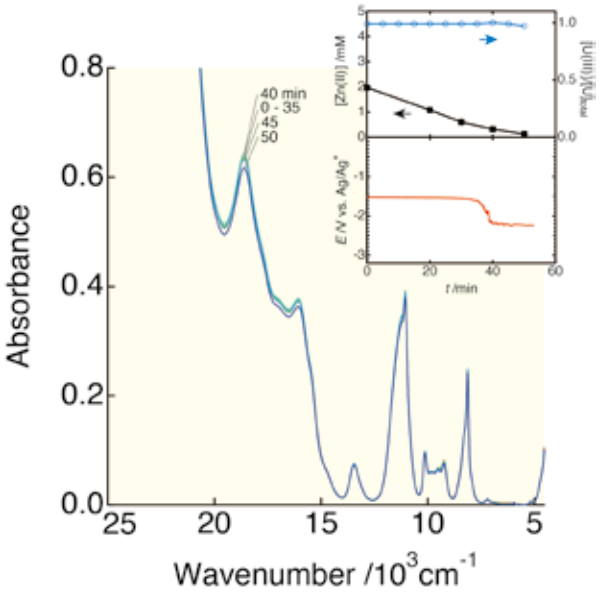

Fig. 1 Absorption spectra during electroseparation of zinc (II) from DMF containing 4.5 mM uranium triflate after reduction by Zn(Hg). Inset shows changes in [Zn(II) and [U(III)]/[U]$_{total}$ (upper) and the electrode potential (lower).

References

[1] C. Tabata, H. Watanabe, K. Shirasaki, A. Sunaga, T. Fukuda, D. Li, and T. Yamamura, J. Mol. Struct. **1277**, 134870 (2023).
[2] K. Shirasaki, J. Appl. Electrochem. **52**, 1101 (2022).

Kenji Shirasaki (Head of Laboratory of Alpha-Ray Emitters)
E-mail: kenji.shirasaki.e4@tohoku.ac.jp
URL: http://alpha.imr.tohoku.ac.jp/en.html

Microstructure and Mechanical Property of Y_2O_3-Based ODS-Cu Alloy Fabricated by MA-HIP with Novel Elemental Addition Process

Analytical Research Core for Advanced Materials

The Analytical Research Core for Advanced Materials serves as an infrastructure for researchers not only in IMR but also outside the university by offering various elemental analytical methods and up-to-date structural characterization techniques. Here, we present recent research carried out by one of our users, where they have elucidated the strengthening mechanism of Cu-based oxide dispersed alloys.

A combination of mechanical alloying and hot isothermal pressing (MA-HIP) is one of the fabrication processes of oxide dispersion strengthened (ODS)-Cu alloy, which is expected to yield a high mechanical property and thermal conductivity. However, the ODS-Cu bulk fabricated MA-HIP process has low ductility due to inhomogeneous oxide dispersion and Cu grain size distribution. In this study, we modified the MA-HIP process by changing yttrium and oxygen addition methods to improve the microstructure and ductility of ODS-Cu alloy. Namely, we replaced pure Y and Cu_2O powders with Cu-Y compound and pre-heated Cu powders as the starting materials [1].

The nanoscale structure was observed by transmission electron microscopy (TEM) and scanning-TEM (STEM) with an acceleration voltage of 200 keV. The electron beam convergence angle and detection angle of a high angle annular dark field (HAADF) STEM is 18-22 mrad and 90-370 mrad, respectively.

Figure 1 (a) shows a HAADF-STEM image of a sample annealed in air. The dark, spherical particles corresponded to Y_2O_3, which appear to be distributed in the large Cu grains as indicated by the circles in (a). As indicated by "A" in (a), coarse precipitates larger than 500 nm are formed in the small Cu grain area, which was found to be coarse Y_2O_3 particles by electron diffraction pattern (b) and high-resolution HAADF-STEM image (c). The magnified image and elemental distribution maps acquired from interface areas of large/small Cu grain areas show that a large amount of fine Y_2O_3 particles is precipitated on grain boundaries, and some of the fine Y_2O_3 particles are also distributed intra-Cu grain.

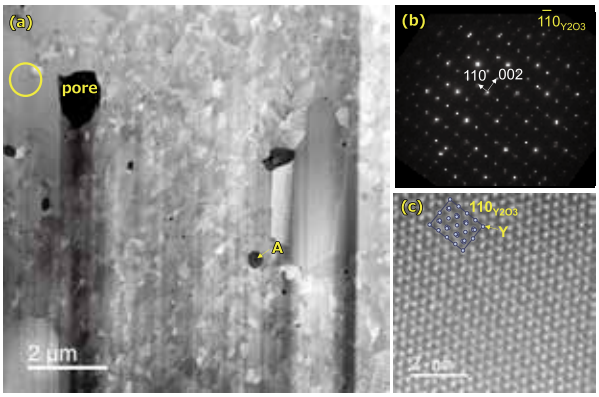

Fig. 1 HAADF-STEM image (a) Some Y_2O_3 particles precipitated, as shown by dark regions, in large Cu grain denoted by a circle. A diffraction pattern (b), and high-resolution HAADF-STEM image (c).

The results presented here hence showed microstructural differences: on the macroscale, the connectivity of large/small Cu grain areas, which was a main factor in brittle fracture, was reduced, while on the nanoscale, yttrium precipitated and remained as yttria (Y_2O_3) particles within the Cu grains. These multiscale microstructural changes resulted on the improved mechanical property: the newly-developed ODS-Cu bulk did not fracture at bending strains of 18% or greater, whereas it had previously fractured at bending strains of 5% or less in a three-point bending test. This improvement in mechanical properties through simple process control suggests that ODS-Cu alloys have further potential as structural materials.

References

[1] Y. Shimada, Y. Nakajima, Y. Hishinuma, K. Ikeda, H. Noto, T. Muroga, K. Yoshida, T. Konno, and Y. Nagai, Mater. Chem. Phys. **307**, 128223 (2023).

Yusuke Shimada (Corresponding Author, Kyushu University)
E-mail: shimada.yusuke.567@m.kyushu-u.ac.jp
Toyohiko J. Konno (Corresponding Author, ARIM Project Unit, Analytical Research Core for Advanced Materials)
Eiji Akiyama (Head of Analytical Research Core for Advanced Materials)
E-mail: eiji.akiyama.d1@tohoku.ac.jp
URL: http://bunseki-core.imr.tohoku.ac.jp/top_eca_eng.html
https://www.imr.tohoku.ac.jp/en/about/divisions-and-centers/service-divisions/03.html

Editors

Public Relations Editorial Committee
Public Relations Office

Printing

HOKUTO Corporation

Organization

Institute for Materials Research
Tohoku University
2-1-1 Katahira, Aoba-ku, Sendai 980-8577, Japan
Tel. +81-(0)22-215-2144 Fax. +81-(0)22-215-2482

URL: https://www.imr.tohoku.ac.jp/
E-mail: pro-adm.imr@grp.tohoku.ac.jp

The latest issue and back issues of KRH are available here.

東北大学 金属材料研究所
Institute for Materials Research
Tohoku University
2-1-1 Katahira, Aoba-ku
Sendai 980-8577, Japan
https://www.imr.tohoku.ac.jp/